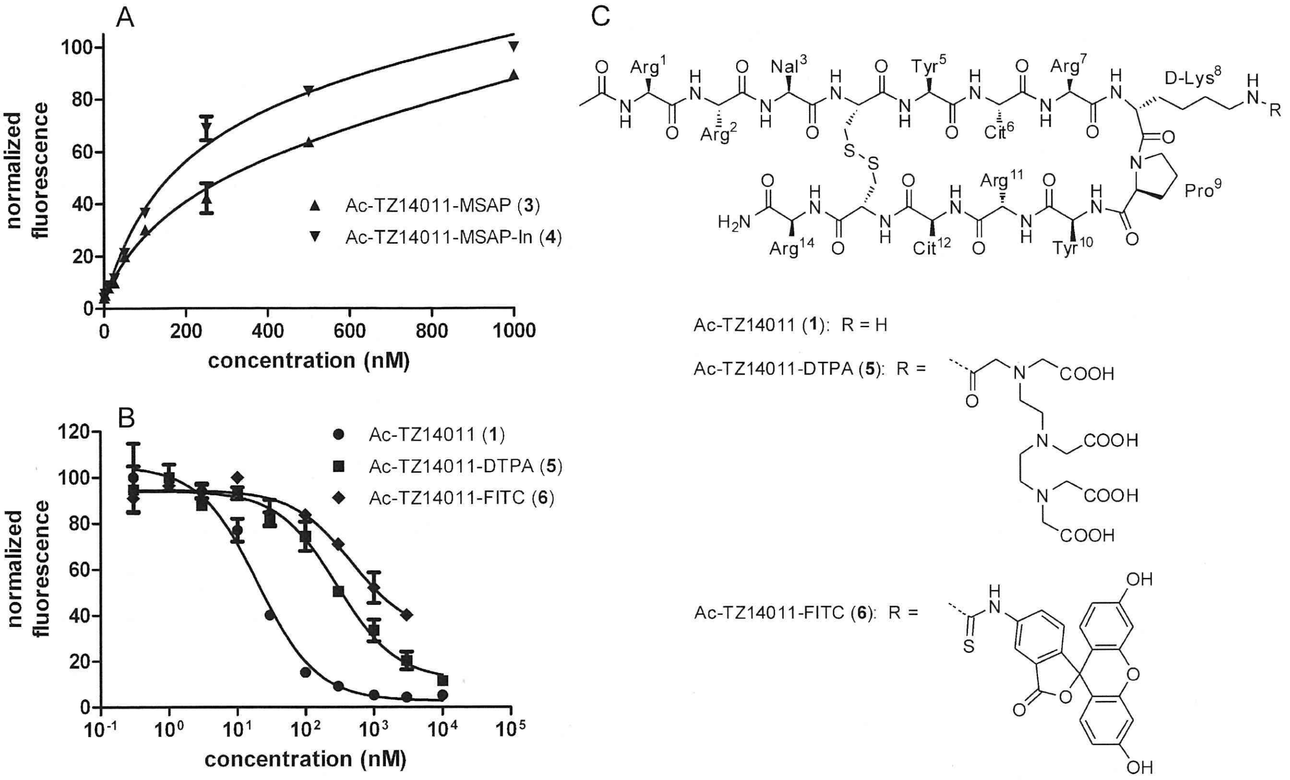

Figure 2. (A) Determination of affinity of constructs **3** and **4** with saturation binding experiments. (B) Competition experiments with three other Ac-TZ14011 peptides in the presence of 250 nM of **3**. (C) Structures of the peptides used for competition experiments.

Table 2. Dissociations Constants (K_D) of the Constructs

construct	K_D (nM)
Ac-TZ14011-unlabeled (**1**)	8.61 ± 1.42
Ac-TZ14011-MSAP (**3**)	186.9 ± 52.4
Ac-TZ14011-MSAP-In (**4**)	177.1 ± 37.2
Ac-TZ14011-DTPA (**5**)	124.4 ± 23.9
Ac-TZ14011-FITC (**6**)	203.5 ± 67.1
TR14010 (**7**)	>5000

was performed at 4 °C to minimize the initial metabolic activity. During imaging at 37 °C, minor staining in vesicular structures was detected. Vesicular internalization is common for liganded membrane receptors, and this form of signal accumulation in the cells proves the potential of using CXCR4 as a target in molecular imaging applications.

Initial *in vivo* studies were performed to evaluate the tumor targeting. Therefore, mice with CXCR4 positive "spontaneous" MIN-O tumors were used instead of the $\mathrm{MDAMB231}^{\mathrm{CXCR4+}}$ cell line, because the CXCR4 expression in $\mathrm{MDAMB231}^{\mathrm{CXCR4+}}$ cells decreases to basal levels *in vivo*. Mice were injected with ^{111}In-labeled Ac-TZ14011-MSAP, and after 24 h, the mice were imaged with SPECT/CT and fluorescence imaging (Figure 4). Both imaging modalities showed high tumor uptake.

For biodistribution studies, we again used mice with CXCR4 positive MIN-O tumors and mice with CXCR4 negative 4T1 tumors as negative control (both tumors had a murine background to prevent xenograph effects) (Table 3). The tumor-to-muscle ratio for the MIN-O tumor was 4.55 ± 0.68, and for the 4T1 tumor, it was 1.20 ± 0.12 ($p < 0.01$), indicating that Ac-TZ14011-MSAP can be used to discriminate CXCR4 positive from CXCR4 negative tumors *in vivo*.

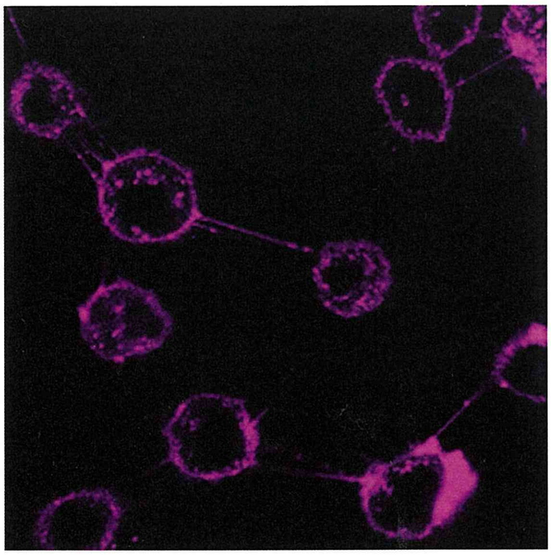

Figure 3. Confocal microscopy of Ac-TZ14011-MSAP (**3**) using $\mathrm{MDAMB231}^{\mathrm{CXCR4+}}$ cells.

In conclusion, we report the first bifunctional CXCR4 antagonistic peptide, containing a Cy5.5-like dye and a DTPA chelate. Despite the functionalization with a relatively large MSAP label, *in vitro* the Ac-TZ14011 derivative retains its specificity and has a high CXCR4-affinity. Moreover, indium binding to the chelate does not affect the fluorescent properties. The initial *in vivo*

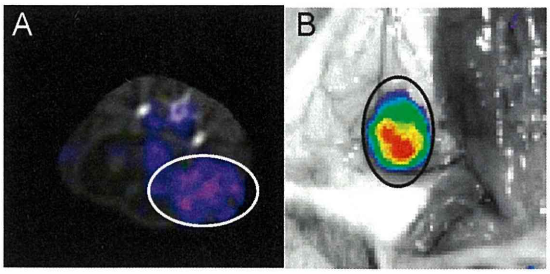

Figure 4. (A) SPECT/CT (axial) and (B) surgical fluorescence image of a MIN-O tumor bearing mouse.

Table 3. Biodistribution of Ac-TZ14011-MSAP in FVB Mice

tissue	uptake (%ID/g)
blood	0.13 ± 0.02
brain	0.02 ± 0.00
lungs	0.93 ± 0.12
heart	0.83 ± 0.20
liver	19.46 ± 4.84
kidneys	6.89 ± 1.29
spleen	4.38 ± 1.16
stomach	0.75 ± 0.14
intestines	1.70 ± 0.08
muscle	0.29 ± 0.01

studies showed the potential of Ac-TZ14011-MSAP for image guided surgery applications.

■ ASSOCIATED CONTENT

Ⓢ Supporting Information. Experimental procedures and spectra of **3** and **4**. This material is available free of charge via the Internet at http://pubs.acs.org.

■ AUTHOR INFORMATION

Corresponding Author

*E-mail: fw.v.leeuwen@nki.nl.

Author Contributions

#These authors contributed equally to this work.

■ ACKNOWLEDGMENT

This research is supported, in part, by a KWF-translational research award (Grant No. PGF 2009-4344; FvL), and within the framework of CTMM, the Centre for Translational Molecular Medicine (http://www.ctmm.nl), project Breast CARE (grant 030-104; JK).

■ REFERENCES

(1) Furusato, B., Mohamed, A., Uhlen, M., and Rhim, J. S. (2010) CXCR4 and cancer. *Pathol. Int. 60*, 497–505.

(2) Bhandari, D., Robia, S. L., and Marchese, A. (2009)The E3 ubiquitin ligase atrophin interacting protein 4 binds directly to the chemokine receptor CXCR4 via a novel WW domain-mediated interaction. *Mol. Biol. Cell 20*, 1324–1339.

(3) Kang, H., Watkins, G., Douglas-Jones, A., Mansel, R. E., and Jiang, W. G. (2005)The elevated level of CXCR4 is correlated with nodal metastasis of human breast cancer. *Breast 14*, 360–367.

(4) Kulbe, H., Levinson, N. R., Balkwill, F., and Wilson, J. L. (2004) The chemokine network in cancer—much more than directing cell movement. *Int. J. Dev. Biol. 48*, 489–496.

(5) Balkwill, F. (2004)The significance of cancer cell expression of the chemokine receptor CXCR4. *Semin. Cancer Biol. 14*, 171–179.

(6) Teicher, B. A., and Fricker, S. P. (2010)CXCL12 (SDF-1)/CXCR4 pathway in cancer. *Clin. Cancer Res. 16*, 2927–2931.

(7) Lazennec, G., and Richmond, A. (2010)Chemokines and chemokine receptors: new insights into cancer-related inflammation. *Trends Mol. Med. 16*, 133–144.

(8) Nimmagadda, S., Pullambhatla, M., Stone, K., Green, G., Bhujwalla, Z. M., and Pomper, M. G. (2010)Molecular imaging of CXCR4 receptor expression in human cancer xenografts with [^{64}Cu]-AMD3100 positron emission tomography. *Cancer Res. 70*, 3935–3944.

(9) Han, Y., Yin, D., Zheng, M., Zhou, W., Lee, Z., Zhan, L., Ma, Y., Wu, M., Shi, L., Wang, N., Lee, J., Wang, C., Lee, Z., and Wang, Y. (2010) Synthesis and preliminary evaluation of a novel ^{125}I-labeled T140 analog for quantitation of CXCR4 expression. *J. Radioanal. Nucl. Chem. 284*, 279–286.

(10) Mather, S. (2009)Molecular imaging with bioconjugates in mouse models of cancer. *Bioconjugate Chem. 20*, 631–643.

(11) Jennings, L. E., and Long, N. J. (2009)'Two is better than one'—probes for dual-modality molecular imaging. *Chem. Commun.* 3511–3524.

(12) Louie, A. (2010)Multimodality imaging probes: design and challenges. *Chem. Rev. 110*, 3146–3195.

(13) Kuil, J., Velders, A. H., and Van Leeuwen, F. W. B. (2010) Multimodal tumor-targeting peptides functionalized with both a radio- and a fluorescent-label. *Bioconjugate Chem. 21*, 1709–1719.

(14) Culver, J., Akers, W., and Achilefu, S. (2008)Multimodality molecular imaging with combined optical and SPECT/PET modalities. *J. Nucl. Med. 49*, 169–172.

(15) Buckle, T., Chin, P. T., van den Berg, N. S., Loo, C. E., Koops, W., Gilhuijs, K. G., and van Leeuwen, F. W. (2010)Tumor bracketing and safety margin estimation using multimodal marker seeds: a proof of concept. *J. Biomed. Opt. 15*, 056021.

(16) Buckle, T., van Leeuwen, A. C., Chin, P. T. K., Janssen, H., Muller, S. H., Jonkers, J., and van Leeuwen, F. W. B. (2010)A self-assembled multimodal complex for combined pre- and intraoperative imaging of the sentinel lymph node. *Nanotechnology 21*, 355101.

(17) Van der Poel, H. G., Buckle, T., Brouwer, O. R., Valdés Olmos, R. A., and Van Leeuwen, F. W. B. (2011)Intraoperative laparoscopic fluorescence guidance to the sentinel lymph node in prostate cancer patients; clinical proof of concept of an integrated functional imaging approach using a multimodal tracer. *Eur. Urol.*, doi:10.1016/j.eururo.2011.03.024.

(18) Tamamura, H., Omagari, A., Hiramatsu, K., Gotoh, K., Kanamoto, T., Xu, Y., Kodama, E., Matsuoka, M., Hattori, T., Yamamoto, N., Nakashima, H., Otaka, A., and Fujii, N. (2001)Development of specific CXCR4 inhibitors possessing high selectivity indexes as well as complete stability in serum based on an anti-HIV peptide T140. *Bioorg. Med. Chem. Lett. 11*, 1897–1902.

(19) Tamamura, H., Hiramatsu, K., Kusano, S., Terakubo, S., Yamamoto, N., Trent, J. O., Wang, Z., Peiper, S. C., Nakashima, H., Otaka, A., and Fujii, N. (2003)Synthesis of potent CXCR4 inhibitors possessing low cytotoxicity and improved biostability based on T140 derivatives. *Org. Biomol. Chem. 1*, 3656–3662.

(20) Tamamura, H., Sugioka, M., Odagaki, Y., Omagari, A., Kan, Y., Oishi, S., Nakashima, H., Yamamoto, N., Peiper, S. C., Hamanaka, N., Otaka, A., and Fujii, N. (2001)Conformational study of a highly specific CXCR4 inhibitor, T140, disclosing the close proximity of its intrinsic pharmacophores associated with strong anti-HIV activity. *Bioorg. Med. Chem. Lett. 11*, 359–362.

(21) Trent, J. O., Wang, Z. X., Murray, J. L., Shao, W., Tamamura, H., Fujii, N., and Peiper, S. C. (2003)Lipid bilayer simulations of CXCR4 with inverse agonists and weak partial agonists. *J. Biol. Chem. 278*, 47136–47144.

(22) Wu, B., Chien, E. Y. T., Mol, C. D., Fenalti, G., Liu, W., Katritch, V., Abagyan, R., Brooun, A., Wells, P., Bi, F. C., Hamel, D. J., Kuhn, P., Handel, T. M., Cherezov, V., and Stevens, R. C. (2010)Structures of the CXCR4 chemokine GPCR with small-molecule and cyclic peptide antagonists. *Science 330,* 1066–1071.

(23) Nomura, W., Tanabe, Y., Tsutsumi, H., Tanaka, T., Ohba, K., Yamamoto, N., and Tamamura, H. (2008)Fluorophore labeling enables imaging and evaluation of specific CXCR4-ligand interaction at the cell membrane for fluorescence-based screening. *Bioconjugate Chem. 19,* 1917–1920.

(24) Oishi, S., Masuda, R., Evans, B., Ueda, S., Goto, Y., Ohno, H., Hirasawa, A., Tsujimoto, G., Wang, Z., Peiper, S. C., Naito, T., Kodama, E., Matsuoka, M., and Fujii, N. (2008)Synthesis and application of fluorescein- and biotin-labeled molecular probes for the chemokine receptor CXCR4. *ChemBioChem 9,* 1154–1158.

(25) Hanaoka, H., Mukai, T., Tamamura, H., Mori, T., Ishino, S., Ogawa, K., Iida, Y., Doi, R., Fujii, N., and Saji, H. (2006)Development of a ^{111}In-labeled peptide derivative targeting a chemokine receptor, CXCR4, for imaging tumors. *Nucl. Med. Biol. 33,* 489–494.

(26) Nishizawa, K., Nishiyama, H., Oishi, S., Tanahara, N., Kotani, H., Mikami, Y., Toda, Y., Evans, B. J., Peiper, S. C., Saito, R., Watanabe, J., Fujii, N., and Ogawa, O. (2010)Fluorescent imaging of high-grade bladder cancer using a specific antagonist for chemokine receptor CXCR4. *Int. J. Cancer 127,* 1180–1187.

(27) Garanger, E., Aikawa, E., Reynolds, F., Weissleder, R., and Josephson, L. (2008)Simplified syntheses of complex multifunctional nanomaterials. *Chem. Commun.* 4792–4794.

(28) Garanger, E., Blois, J., Hilderbrand, S. A., Shao, F., and Josephson, L. (2010)Divergent oriented synthesis for the design of reagents for protein conjugation. *J. Comb. Chem. 12,* 57–64.

(29) Shao, F., Yuan, H., Josephson, L., Weissleder, R., and Hilderbrand, S. A. (2011)Facile synthesis of monofunctional pentamethine carbocyanine fluorophores. *Dyes Pigments 90,* 119–122.

(30) Moulin, C., Amekraz, B., Steiner, V., Plancque, G., and Ansoborlo, E. (2003)Speciation studies on DTPA using the complementary nature of electrospray ionization mass spectrometry and time-resolved laser-induced fluorescence. *Appl. Spectrosc. 57,* 1151–1161.

(31) Maecke, H. R., Riesen, A., and Ritter, W. (1989)The molecular structure of indium-DTPA. *J. Nucl. Med. 30,* 1235–1239.

(32) Schottelius, M., and Wester, H. J. (2009)Molecular imaging targeting peptide receptors. *Methods 48,* 161–177.

Am J Nucl Med Mol Imaging 2012;2(1):99-109
www.ajnmmi.us /ISSN:2160-8407/ajnmmi1110003

Original Article

Non-invasive longitudinal imaging of tumor progression using an ^{111}indium labeled CXCR4 peptide antagonist

Tessa Buckle[1,2], Nynke S van den Berg[1,2], Joeri Kuil[1,2], Anton Bunschoten[1,2], Joppe Oldenburg[1], Alexander D Borowsky[3], Jelle Wesseling[4], Ryo Masada[5], Shinya Oishi[5], Nobutaka Fujii[5], Fijs WB van Leeuwen[1,2]

[1]Departments of Radiology and Nuclear Medicine, The Netherlands Cancer Institute - Antoni van Leeuwenhoek Hospital (NKI-AvL), Amsterdam, The Netherlands; [2]Department of Radiology, Interventional Molecular Imaging group, Leiden University Medical Center (LUMC), Leiden, The Netherlands; [3]Department of Pathology and Laboratory Medicine, Center for Comparative Medicine, School of Medicine, University of California at Davis, Sacramento, US; [4]Department of Pathology, The Netherlands Cancer Institute - Antoni van Leeuwenhoek Hospital (NKI-AvL), Amsterdam, The Netherlands; [5]Graduate School of Pharmaceutical Sciences, Kyoto University, Kyoto, Japan

Received October 28, 2011; accepted November 5, 2011; Epub December 15, 2011; Published January 1, 2012

Abstract: The chemokine receptor 4 (CXCR4) is a biomarker that is over-expressed in ductal carcinoma in situ (DCIS). Hence, CXCR4-targeted (molecular) imaging approaches may have diagnostic value in such a challenging, premalignant lesion. The indium labeled CXCR4 peptide-antagonist, ^{111}In-DTPA-Ac-TZ14011, was used to visualize CXCR4-expression in a mammary intraepithelial neoplastic outgrowth (MIN-O) mouse tumor model resembling human DCIS. MIN-O lesion development was longitudinally monitored using SPET/CT and tracer uptake was compared to uptake in control lesions. Expression of CXCR4 was validated using immunohistochemistry and flow cytometric analysis. The uptake of ^{111}In-DTPA-Ac-TZ14011 was related to tumor angiogenesis using ^{111}In-cDTPA-[RGDfK]. Twenty-four hours after tracer injection, MIN-O lesions could be discriminated from low CXCR4-expressing control tumors, while the degree of angiogenesis based on the $\alpha_v\beta_3$ integrin expression in both tumor types was similar. The uptake of ^{111}In-DTPA-Ac-TZ14011 in early MIN-O lesions was significantly lower than in larger intermediate and late-stage lesions, two-and-a-half-times ($p=0.03$) and seven-times ($p=0.002$), respectively. Intermediate and late stage lesions show a higher degree of membranous CXCR4-staining at immunohistochemistry and flow cytometric analysis. From this study we can conclude that ^{111}In-DTPA-Ac-TZ14011 can be used to visualize the CXCR4-expression in MIN-O lesions longitudinally.

Keywords: Chemokine receptor 4 (CXCR4), ductal carcinoma in situ (DCIS), single photon emission computed tomography (SPECT), mouse model, tumor progression, longitudinal imaging

Introduction

The chemokine receptor 4 (CXCR4) was first identified as co-receptor for infection of lymphocytes in HIV [1] and was later also found to be over-expressed in breast, prostate and ovarian cancer, as well as in numerous other cancer types [2]. CXCR4 over-expression has been linked to increased tumor aggressiveness and invasiveness [3] and was therefore mentioned as a possible target for therapy [4,5].

Another possible clinical application of CXCR4 as a target is the visualization of breast cancer lesions such as ductal carcinoma in situ (DCIS). Salvucci et al. [6] reported that 69% of the DCIS lesions evaluated in their patient study was CXCR4-positive at immunohistochemistry (IHC), whereas Schmid et al. [7] reported a 92% positivity rate. Non-invasive visualization of DCIS is clinically challenging; X-ray mammography and contrast enhanced magnetic resonance imaging (MRI) do not always accurately detect DCIS [8-10]. Hence, CXCR4 targeting imaging probes are expected to help improve clinical diagnostics.

Numerous efforts are currently being conducted in the development of small molecules that target CXCR4 e.g. AMD3100 [11, 12] and antagonistic peptides e.g. T140 [13]. Derivatives of the T140 antagonistic peptide, such as Ac-TZ14011 are more potent and bio-stable [14, 15]. Furthermore, these peptides are very versatile imaging platforms as addition of various diagnostic labels is possible without interfering with the pharmacophore [16-20]. An example of such a compound is ^{111}In-DTPA-Ac-TZ14011 [21].

The well described mammary intraepithelial neoplastic outgrowth (MIN-O) model, a mouse model resembling human DCIS [22, 23] has been previously used in imaging studies [21]. In this model, preinvasive lesions progress to invasive lesions [24, 25]. Progression is consistent over time, and, conveniently, progression into the invasive phenotype results in palpable lesions. Differences in tumor cell differentiation, gene expression, and metabolism associated with progression have been reported, and these features also correspond to similar features in human DCIS progression to carcinoma.

We have used the preclinical MIN-O model and a low CXCR4-expressing negative 4T1 tumor model to evaluate the ability of ^{111}In-DTPA-Ac-TZ14011 to longitudinally visualize the progression of the tumor lesions via their CXCR4-expression. The imaging results were compared to immunohistochemical and flow cytometric analysis of the tumor tissue. Furthermore, we used ^{111}In-DTPA-c[RGDfK] to determine the influence of angiogenesis on the uptake of ^{111}In-DTPA-Ac-TZ14011 in both tumor models.

Materials and methods

In vivo mouse model

For generation of the MIN-O tumor lesions, FVB mice (n=20; 3-4 weeks of age) were used. Before transplantation (and imaging), mice were anaesthetized using a hypnorm (VetaPharma Ltd)/dormicum (Midazolam; Roche)/water solution (1:1:2; 5µl/g i.p.). Via a small incision, the inguinal lymph node was excised where after a piece of preinvasive MIN-O tissue (line 8w-B) [25] was placed into the remaining tissue of the fourth mammary gland. Approximately 3 weeks after transplantation, lesions were deemed suitable for further experiments.

Control experiments were performed using orthotopic transplantation of 0.25×10^5 4T1 tumor cells into the mammary tissue of Balb/c nude mice (n=20; 6-8 weeks of age). 4T1 cells were cultured under standard conditions in MEM medium containing MEM vitamins, L-glutamine, non-essential amino acids, natrium/pyruvate and penicillin/streptomycin solution (all BD Biosciences). Before transplantation, cells were trypsinized and washed with HBSS (BD Biosciences). Transplantation of cells was carried out under identical conditions as placement of the MIN-O segments. All animal experiments were performed in accordance with Dutch welfare regulations and approved by the local ethics committee.

Radiolabeling of DTPA-Ac-TZ14011

DTPA-Ac-TZ14011 (**Figure 1A**) was synthesized as previously described by Hanaoka et al. [21]. For imaging of one mouse, 50µg of the DTPA- Ac -TZ14011 peptide antagonist was dissolved in 80µl 0.1M acetic acid and 20µl $^{111}InCl_3$ (10 MBq; Covidien-Mallinkrodt) was added. After 30 minutes of incubation, labeling was validated using thin layer chromatography. In all cases, labeling efficacy was >99%. Before injection, 1ml of saline was added. For synthesis and radiolabeling of DTPA-c[RGDfK] and DTPA-4F-Bz-TZ14011 (a different CXCR4 targeting peptide of the T140 family, here used as reference peptide), see Supporting information.

Imaging using SPECT/CT

Mice were injected intravenously with 50µg ^{111}In-DTPA-Ac-TZ14011 antagonist (10 MBq) or with 25µg ^{111}In-DTPA-c[RGDfK] (10 MBq). SPECT/CT scans were conducted as described previously [26] on a preclinical SPECT/CT scanner (Nanospect; Bioscan) at 1 hour and 24 hours post injection. After acquisition, the CT data was reconstructed using a cone-beam filtered back projection and SPECT data were reconstructed using iteratively with HiSPECT software (Scvis GmbH). Signal intensities were analyzed using the InVivoScope post-processing software (Bioscan, Inc.) [26]. CT images were used to perform size measurements on the tumor. The formula for ellipsoid shapes: $3/4\pi \times ((1/2a)x(1/2b)x(1/2c))$ was used to calculate the tumor volume.

Tumor stages were differentiated by size and histology. Size limits for the different stages were based on values reported by Abbey et al. [23] and correlations between tumor volume and immunohistochemistry using our own data. Tumor lesions <100 mm^3 were deemed as early

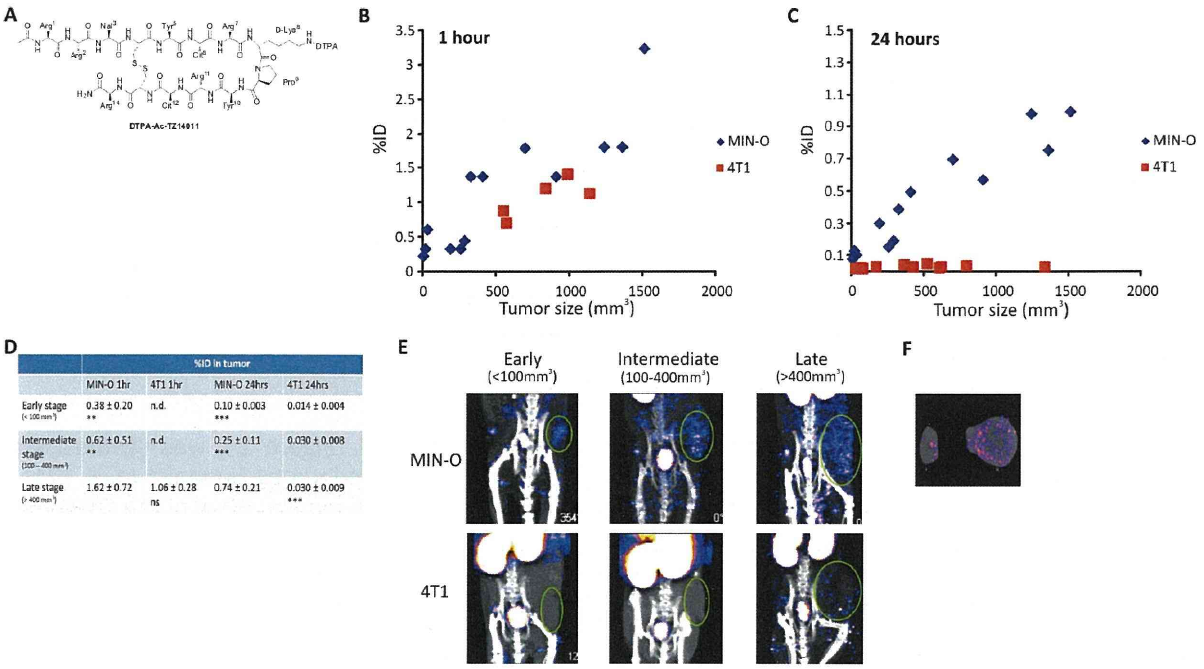

	%ID in tumor			
	MIN-O 1hr	4T1 1hr	MIN-O 24hrs	4T1 24hrs
Early stage (< 100 mm³)	0.38 ± 0.20 **	n.d.	0.10 ± 0.003 ***	0.014 ± 0.004
Intermediate stage (100 – 400 mm³)	0.62 ± 0.51 **	n.d.	0.25 ± 0.11 ***	0.030 ± 0.008
Late stage (> 400 mm³)	1.62 ± 0.72	1.06 ± 0.28 ns	0.74 ± 0.21	0.030 ± 0.009 ***

Figure 1. Longitudinal SPECT/CT imaging of ^{111}In-DTPA-AC-TZ14011. A) Chemical structure of DTPA-Ac-TZ14011. Tumor uptake of ^{111}In-DTPA-Ac-TZ14011 measured at B) 1 hour and C) 24 hours after injection was set out against the tumor volume. D) Uptake in tumors within the same size range was compared. E) SPECT/CT images (MIP) of MIN-O and 4T1 tumor lesions at 24 hours after injection. F) Ex vivo tracer distribution in a 4T1 (i) and MIN-O (ii) tumor lesion after SPECT/CT imaging. Significance between uptake values was determined using a T-test. Not significant was noted as ns, p-values < 0.02 for comparison with late stage MIN-O lesions were noted as ** and p-values < 0.002 as ***. n.d. = not determined.

stage, lesions between 100 and 400 mm³ were deemed as intermediate stage, and >400 mm³ as late stage lesions. In the mice that were longitudinally followed, it was only possible to determine the percentage of the injected dose (% ID), as the weight of the tumor was unknown. Moreover, the density of the lesions differs between stages and tumors. For these reasons corrections based on tumor volume were considered inaccurate.

In a region of interest including only the tumor, the %ID was calculated ((MBq measured in tissue/ injected dose) *100%) and MIN-O and 4T1 tumors within the same size range were compared. After the final SPECT/CT scan mice were sacrificed and organs and tumors were excised and weighed to determine the percentage of the injected dose per gram (%ID/g). The amount of radioactivity present in the tissue was counted using a gamma counter (Wizard 3" 1480 automatic gamma counter, Perkin Elmer; 245kev; 60sec). The ID/g was calculated as followed: ((MBq measured in tissue/injected dose) *100%)/weight of tissue. Statistics were conducted using a standard T-test.

Immunohistochemistry (IHC)

Formalin fixed paraffin embedded MIN-O or 4T1 tumor tissue sections were stained according to the protocol previously reported by van den Berg et al. [20] with a monoclonal anti-CXCR4 antibody (Rat-anti-CXCR4 clone 2B11 1:100; BD Biosciences). Slides were assessed by a consultant breast pathologist and scored as positive or negative for the cell membrane and cytoplasm staining. Images were taken with a color CCD microscope system (Axiovert S100 with AxiocamHRc, Carl Zeiss) at a 25x or 40x magnification.

The percentage of cytoplasmic or membranous staining per slide was determined by dividing the amount of stained cells in a specific area by the total amount of cells in that area and multiplying this by 100%. Per tumor type/stage five different tumor slides were assessed. Per slide, five different areas were evaluated (magnification 40x). The ratio between the MIN-O and 4T1 tumors was determined by dividing the percentage of membranous staining in the MIN-O tumor lesions by the percentage of membranous staining in the 4T1 tumor lesions.

For the MIN-O model, early, intermediate, and late stage tumors were assessed. For the 4T1 tumor model, only large tumors (corresponding in size with late stage MIN-O lesions) were assessed as CXCR4 expression levels between different stages of 4T1 lesions did not differ. Increase in membranous staining in the different MIN-O tumor stages was determined by dividing the percentage of staining in the intermediate or late stage MIN-O tumor lesions by the percentage of staining of the early stage MIN-O tumor lesions. Statistics were performed using a standard T-test.

Flow cytometry

Tumor bearing mice were sacrificed and the tumor was excised and a single cell suspensions were made. All stages of MIN-O lesions were assessed. Again, for the 4T1 tumor model, only late stage tumors were used as the CXCR4 expression levels between different stages of 4T1 lesions did not differ. Cell-suspensions were incubated for 5 minutes with an ER-lysis buffer (0.31M NH_4Cl, 0.02M $KHCO_3$, 0.5M EDTA in 2L H_2O; pH 7.4).

500,000 cells per measuring condition were washed with 0.1% bovine serum albumin in phosphate buffered saline (0.1% BSA/PBS) and incubated for 1hour on ice with monoclonal phycoerythrin (PE) labeled anti-CXCR4 antibody 2B11 (2B11-PE; 1:100; BD Biosciences) to determine their CXCR4 expression levels. After incubation, cells were washed with 0.1% BSA/PBS after which propidium iodide (PI; 1:10000; BD Biosciences) was added.

For evaluation of the amount of lymphocytes within the CXCR4 positive population in the tumor cell suspensions, cells were co-incubated for 1hour with the 2B11-PE antibody and an Alexafluor700 labeled anti-CD45 antibody (CD45-AF700 clone 30 F11; 1:200; eBioscience). The percentage of CXCR4 positive lymphocytes was determined by dividing the CD45 positive population within the CXCR4 positive population by the total amount cells and multiplying this by 100%.

Antibodies were diluted in 0.1% BSA/PBS in all flow cytometry experiments. Non-antibody incubated cells served as controls. After staining, cells were analyzed using a Beckton Dickinson FACScalibur (BD Biosciences) equipped with Cell Quest Pro software (BD Biosciences). PE fluorescence was detected in the FL2 channel (excitation 488nm; emission filter 530/30nm). PI was detected in the FL3 channel (excitation 488nm; emission > 670nm). AF700 was detected in the FL4 channel (excitation 635nm; emission 668nm).

Mean fluorescent signal intensity ratio's (MFIRs) were calculated as: the mean fluorescent signal intensity antibody incubated condition divided by the mean fluorescent signal intensity of the control (no antibody). Increase in signal in the different MIN-O tumor stages was determined by dividing the MFIR obtained in the intermediate or late stage MIN-O tumor lesions by the MFIR of the early stage MIN-O tumor lesions.

Determination of the binding affinity (KD) of DTPA-Ac-TZ14011 and the reference peptide DTPA-4F-Bz-TZ14011 is described in the Supporting Information. Statistics were performed using a standard T-test. All experiments were performed at least in triplicate.

Distribution

Mice were injected intravenously with 50μg ^{111}In-DTPA-Ac-TZ14011 (1MBq). Twenty-four hours after injection, mice were sacrificed and tissues were excised. Tissues were weighed and the amount of radioactivity present in the tissues was counted using a gamma counter (Wizard 3” 1480 automatic gamma counter, Perkin Elmer; 245kev; 60sec). Counts per minute were converted into MBq and corrected for decay. The percentage of the injected dose per gram of tissue (%ID/g) was calculated as followed: ((MBq measured in tissue/ injected dose) *100%) / weight of tissue. Distribution of ^{111}In-DTPA-4F-BzTZ14011 is described in the Supporting information.

Results

To evaluate the potential of ^{111}In-DTPA-Ac-

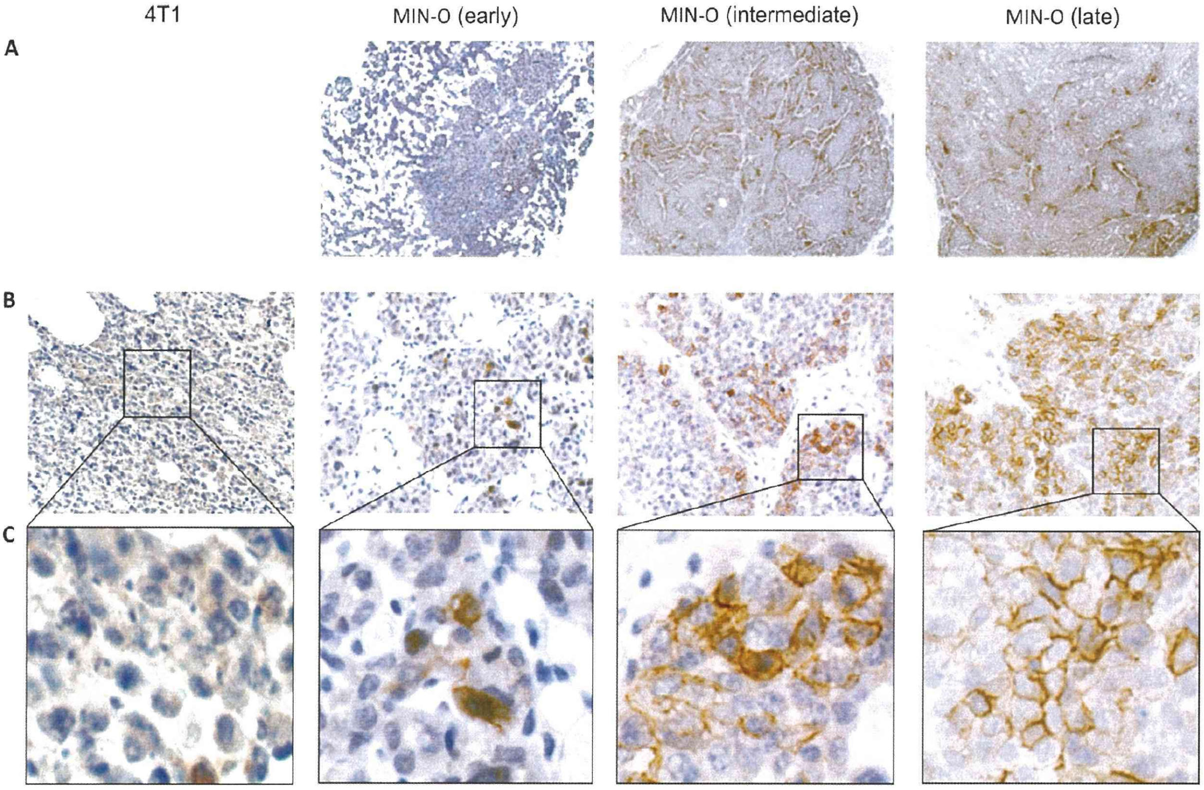

Figure 2. Immunohistochemistry: CXCR4 staining in 4T1 and MIN-O tumor tissue. A) Distribution of the CXCR4 staining of the different MIN-O tumor stages. B) At a 25x magnification, in 4T1 tumor tissue only cytoplasmatic staining can be seen. In MIN-O tumor tissue, next to cytoplasmatic staining, an increasing level of membranous staining is observed. C) Membranous staining at 40x magnification.

TZ14011 to visualize CXCR4-expression in the tumor lesions, a group of animals was scanned longitudinally using microSPECT/CT (**Figure 1**). Mice were scanned when tumors were <100 mm^3 (early stage), 100-400 mm^3 (intermediate stage) and >400 mm^3 (late stage) in size. Lesions as small as 10 mm^3 could be identified using SPECT/CT.

Because incubation time of the agent can affect the imaging outcome, the optimal incubation time was evaluated by comparing the tumor uptake at 1 hour and 24 hours post injection. At 1 hour post injection MIN-O tumor lesions could be detected but differences between CXCR4 positive (MIN-O) and control (4T1) tumors were not apparent (**Figure 1B**). Uptake in late stage MIN-O lesions was higher than the uptake (%ID) in 4T1 tumor lesions at 1 hour post injection, however, this difference was not significant (**Figure 1D**). Uptake in the tumor lesions at 24 hours post injection had overall decreased, but at this time differences between the MIN-O and 4T1 lesions were highly significant (**Figure 1C/D**). More importantly, uptake in 4T1 tumor lesions was low in tumors of all sizes (between 0.014 ± 0.004%ID to 0.030 ± 0.009%ID), whereas the uptake in MIN-O lesions increased with lesion size (**Figure 1D**). Uptake increased from 0.10 ± 0.03% of the injected dose in early stage lesions to 0.25 ± 0.11% in intermediate stage and 0.74 ± 0.21% in late stage MIN-O lesions. Uptake levels in MIN-O tumor lesions larger than 10mm^3 exceeded uptake levels found in 4T1 tumors with a size range of 10-1338 mm^3. **Figure 1E** shows SPECT/CT images of the lesions during the different stages of tumor progression of both 4T1 and MIN-O tumor lesions. After the final SPECT/CT scan in the series, the %ID/g was determined. This resulted in a higher value in late stage MIN-O tumor lesions (0.27 ± 0.06) compared 4T1 lesions of comparable size (0.14 ± 0.02; $p=0.05$). The tumor-to-muscle-ratio (T/M) was 1.5 fold higher in the late stage MIN-O tumors; 7.17 ± 0.47 compared to 4.75 ± 0.90 in 4T1 tumors (p=0.01). Ex vivo SPECT/CT measurements show the distribution throughout the tumor in the two tumor types (**Figure 1F**).

To validate that the tumor uptake during SPECT/CT imaging can be correlated to CXCR4-expression, we evaluated the level of CXCR4-expression in the different tumor tissues by IHC. Slices of MIN-O and 4T1 tumor tissue were stained using the 2B11 anti-CXCR4 antibody and cytoplasmatic and membranous staining levels were analyzed. In MIN-O lesions, staining patterns varied between different areas in the tumor, showing clear CXCR4 positive and negative areas (**Figure 2A**) and when compared to the low CXCR4-expressing 4T1 tumor tissues, a different staining pattern was found (**Figure 2B**). Further evaluation demonstrated that in MIN-O lesions, CXCR4 staining was located in the cytoplasm and on the membrane of the tumor cells (**Figure 2C**). 4T1 and early stage MIN-O lesions showed predominantly cytoplasmic staining and only sporadic membranous staining for CXCR4. Membranous staining was more evident in the larger intermediate stage MIN-O lesions and most apparent in the largest MIN-O lesions investigated.

This visual observation was further underlined by quantitative analysis of the stained tissue slides. In **Table 1**, the percentage of CXCR4 staining determined by IHC in the different MIN-O stages and in the 4T1 control tumors is shown. No significant difference in cytoplasmatic staining was observed between the different tumor lesions, but differences in percentages of membranous staining were apparent.

While membranous staining in 4T1 and early stage MIN-O lesions was almost identical (3.8 ± 1.9% and 4.1 ± 2.3%), the percentage of membranous staining increased 3.3 times in intermediate and 5.1 times in late stage MIN-O lesions compared to the early stage MIN-O lesions. As only one representative slide per tumor was evaluated, this contributed to the relatively high Standard Deviation (SD) in the quantitative analysis of the staining percentages (**Table 1**).

Table 1. Quantitative analysis of CXCR4 staining. Tumor cells were counted under 40x magnification (n=5 per tumor type). Percentage cytoplasmic and membranous staining was calculated by dividing the amount of stained cells in an area by the total amount of cells counted in that area and multiplying this by 100%. P-values <0.05 for comparison with late stage MIN-O lesions were noted as ** and p-values <0.01 as ***.

Tumor type	% Cytoplasmic staining	% Membranous staining
MIN-O Early stage (<100mm^3)	81.1 ± 10.6	4.1 ± 2.3 ***
MIN-O Intermediate stage (100-400mm^3)	84.8 ± 8.6	13.5 ± 5.8 **
MIN-O Late stage (>400mm^3)	90.6 ± 3.3	21.0 ± 8.0
4T1 Late stage (>400mm^3)	92.2 ± 3.0	3.8 ± 1.9 ***

Further evaluation of the membranous CXCR4 expression in the tumor lesions was conducted by flow cytometric analysis. Viable tumor cells were incubated with a PE-labeled version of the anti-CXCR4 antibody that was used for IHC. By performing the labeling on ice the metabolic activity of the cells is slowed down preventing endocytosis, enabling visualization of only the cell-membrane-receptor-bound signal. Therefore, the level of fluorescence that could be detected in the tumor cell suspensions provided a measure of the membranous CXCR4-expression. Similar to results obtained with IHC (See **Table 1**), a clear difference between the level of CXCR4 expression in the 4T1 and MIN-O tumors was found (**Table 2**). Mean fluorescent intensity ratio's (MFIR) in the MIN-O tumor cells increased with tumor progression. The MFIR in intermediate and late stage MIN-O tumor cells was respectively 1.9 times and 2.4 times higher than the MFIR in early stage MIN-O tumor cells. In all stages of MIN-O tumor progression, a higher level of fluorescence was detected than in the (late stage) 4T1 tumor cells used in these experiments.

Flow cytometry was also used to determine the binding affinity of DTPA-Ac-TZ14011 (K_D = 37.89 ± 7.87 nM; See Supporting Information). As a reference, binding the affinity of DTPA-4F-Bz-TZ14011 was also determined (K_D = 14.13 ±

Table 2. Flow cytometric analysis of 4T1 and MIN-O tumor cells. Tumor cell-suspensions were incubated with 2B11-PE. The fluorescent signal emitted by CXCR4 positive cells was measured (n=3 per tumor type). The mean fluorescent intensity ratios (MFIR) were determined. The percentage of lymphocytes within the CXCR4 positive population was determined after co-incubation with 2B11-PE and an Alexa-Fluor700 labeled anti-CD45 antibody.

Tumor type	MFIR	%lymphocytes
MIN-O Early stage (<100mm^3)	2.25 ± 0.17	0.43 ± 0.002
MIN-O Intermediate stage (100-400mm^3)	4.32 ± 0.02	2.07 ± 0.001
MIN-O Late stage (>400mm^3)	5.36 ± 1.80	3.48 ± 0.004
4T1 Late stage (>400mm^3)	1.70 ± 1.07	3.39 ± 0.002

Table 3. Distribution of ^{111}In-DTPA-Ac-TZ14011. Mice were killed 24 hours after injection of ^{111}In-DTPA-Ac-TZ14011. Tissues were excised and radioactivity in the tissues was determined using a gamma counter. %ID/g was calculated using the following formula: ((MBq measured in tissue/injected dose) *100%)/weight tissue.

Tissue	%ID/g
Blood	0.02 ± 0.00
Brain	0.00 ± 0.00
Lungs	0.19 ± 0.01
Heart	0.08 ± 0.01
Liver	5.53 ± 0.51
Kidneys	24.82 ± 0.94
Spleen	1.03 ± 0.11
Stomach	0.08 ± 0.01
Intestines	0.16 ± 0.02
Muscle	0.03 ± 0.01
Mammary fatpad	0.05 ± 0.02
Axillary lymph nodes	1.33 ± 0.81

2.67 nM; see Supporting Information). The difference in binding affinity between DTPA-Ac-TZ14011 and DTPA-Bz-TZ14011 was comparable to the two-fold difference recently reported by Jacobsen et al. [17]. Please note that DTPA-Bz-TZ14011 is a derivative of the peptide reported by Jacobsen et al., as such the affinity may differ slightly. For more details regarding the difference between the peptides, see Supporting Information.

Distribution studies at 24 hours post injection revealed that ^{111}In-DTPA-Ac-TZ14011 is predominantly cleared via the kidneys, and to a lesser extent via the liver (**Table 3**). Hanaoka et al. previously reported on the distribution of ^{111}In-DTPA-Ac-TZ14011 which also included a blocking study using unbound peptide [21]. We report the distribution using a different peptide dose but overall, distribution is comparable. No significant differences between the distribution of ^{111}In-DTPA-4F-Bz-TZ14011 and ^{111}In-DTPA-Ac-TZ14011 were observed (See supporting information). T/M ratio's were also similar (6.45 ± 0.15 and 7.17 ± 0.47 respectively).

As can be seen in **Table 3**, tracer uptake is relatively high in the spleen and lymph nodes. These organs are both part of the immune system and are known to harbor large amounts of CXCR4 positive lymphocytes [27]. The presence of such CXCR4 positive lymphocytes in the tumor lesions can also be of influence on uptake levels of ^{111}In-DTPA-Ac-TZ14011. For this reason, we evaluated the level of lymphocytes present within the CXCR4 positive tumor cell population using flow cytometry. Analysis was done after co-incubation of an Alexa Fluor700 labeled anti-CD45 antibody and the PE-labeled anti-CXCR4 antibody (see **Table 2**). The percentage of lymphocytes present in MIN-O tumor tissue increased with size/tumor stage; in early stage tumor cells only 0.43% of the cells in the tumor were CD45 positive, increasing to 2.07% in intermediate and to 3.48% in late stage MIN-O tumors. However, the presence of lymphocytes in late stage 4T1 tumor tissue (3.39%) was comparable to late stage MIN-O tumor tissue. Pathological analysis of tumor slices also revealed very low amounts (≈ 2%) of lymphocytes in the tumor tissue. It is therefore not likely that uptake levels of ^{111}In-DTPA-Ac-TZ14011 in the MIN-O and 4T1 tumor lesions are influenced by the presence of lymphocytes in the tumor.

To further specify that the uptake of ^{111}In-DTPA-

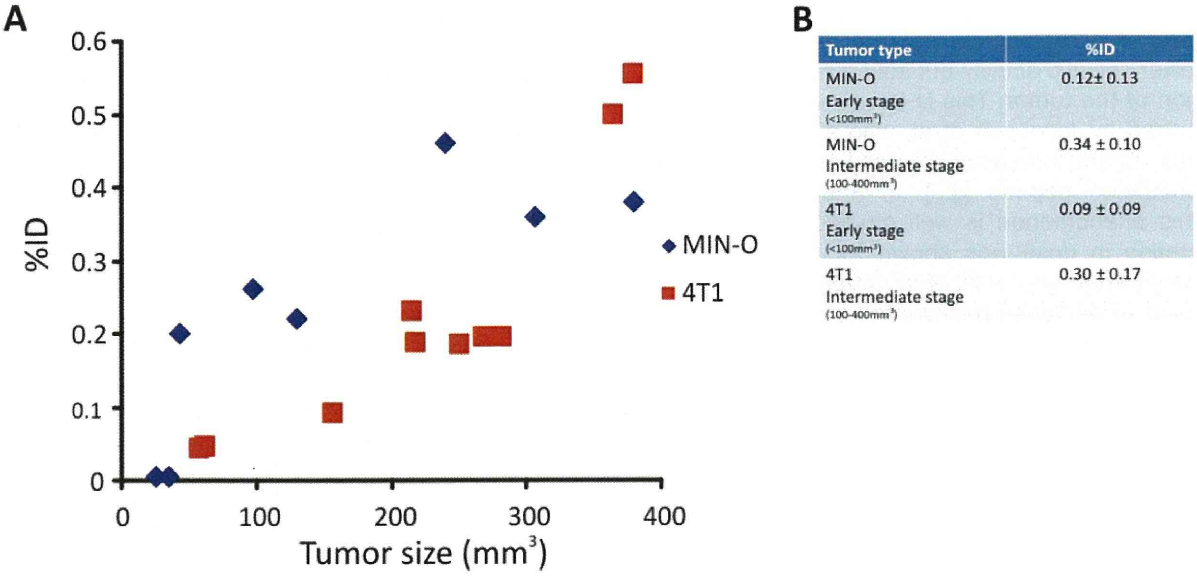

Tumor type	%ID
MIN-O Early stage (<100mm^3)	0.12± 0.13
MIN-O Intermediate stage (100-400mm^3)	0.34 ± 0.10
4T1 Early stage (<100mm^3)	0.09 ± 0.09
4T1 Intermediate stage (100-400mm^3)	0.30 ± 0.17

Figure 3. Longitudinal SPECT/CT imaging of ^{111}In-DTPA-c[RGDfK]. A) Tumor uptake of ^{111}In-DTPA-c[RGDfK] was longitudinally monitored at 24 hours after injection. B) Uptake in tumors of tumors within the same size range were compared.

Ac-TZ14011 in the tumor lesions is related to the level of CXCR4 expression in the tumor cells, factors such as the effect of angiogenesis (based on $\alpha_v\beta_3$ integrin expression) on the uptake had to be excluded. Therefore, we evaluated the uptake of ^{111}In-DTPA-c[RGDfK] in the different tumor models. The RGD peptide, c [RGDfK], binds to $\alpha_v\beta_3$ integrin, of which expression is linked to angiogenesis [28]. Uptake of ^{111}In-c[RGDfK]-DTPA in both MIN-O and 4T1 lesions increased with increasing lesion size and no significant difference in uptake between the models was observed (**Figure 3**).

Discussion

We have studied the potential of ^{111}In-DTPA-Ac-TZ14011 to longitudinally monitor the CXCR4-expression in the MIN-O mouse tumor model that resembles human DCIS. These studies have demonstrated that CXCR4-imaging could be used to monitor progression from small early stage lesions to larger intermediate and late stage lesions.

Rather than using subcutaneous xenograft based models wherein transfected (human) cell lines with extremely high CXCR4 expression rates are used [29], small early stage MIN-O mouse tumor segments were transplanted orthotopically in the mammary fatpad. This transplantation model may resemble human lesion progression more accurately than that of a (CXCR4 transfected) xenograft model. Moreover, in the MIN-O model the CXCR4 expression is in line with the 5-fold over expression reported for in human tumor samples [6]. The difference between high and low CXCR4 expressing lesions will possibly be more black-and -white when transfected cell lines are used, but the CXCR4 expression in these (mostly) homogeneous tumor lesions is likely to have less similarity with the human situation. In the "spontaneous" murine MIN-O model the relatively low CXCR4-expression levels can be accurately detected – a 5.4 fold increase compared to surrounding mammary tissue- and can be differentiated from the cell line based 4T1 control tumor tissues. Also important, CXCR4-expression in MIN-O lesions is heterogeneous. Ex vivo SPECT/CT imaging showed a patchy staining pattern in the tumor (**Figure 1F**) and IHC revealed clear positive and negative area's (**Figure 2A**) in the MIN-O tumor tissue. This heterogeneous presence of CXCR4 is in line with what is seen in breast cancer patient biopsies [7].

Initial SPECT/CT experiments were performed using a lower dose (10 μg; data not shown).

Unfortunately, tumors could not be visualized clearly. Increasing the dose to 50 μg lead to a lower specific activity but also a better visualization of the tumor. This is in line with results reported by Jacobsen et al. who showed that tumor uptake increased after co-injection of 50 μg unlabeled peptide [17]. In antibody- imaging this phenomenon is well studied. Here an increase in dose was shown to improve tumor penetration and unlabeled antibody is generally used to decrease background staining [30-32]. Imaging using SPECT/CT revealed that an ^{111}In-DTPA-Ac-TZ14011 signal could already be detected in MIN-O lesions as small as 10mm^3 and uptake levels in lesions beyond 10mm^3 exceded the uptake in 4T1 control tumors. These findings illustrate the potential of CXCR4-imaging to visualize small lesions. Obviously, ducts in the human mammary gland are not as closely packed as in the mouse model. Hence the value of these findings in a clinical setting still requires further investigation. Our preclinical findings, however, indicate that the signal detected in MIN-O lesions is 7.2-times as high as the signal found in muscle and 5.4-times as high as the signal found in the opposite mammary fat pad. These signal to background ratios should make the tracer uptake diagnostically relevant.

Compared to a human situation the MIN-O mouse model of DCIS progression simplifies these experiments. Nevertheless, in our opinion, the imaging data combined with the reported detection of CXCR4 in human DCIS examples [6, 7] warrants further investigation towards using CXCR4 targeted agents to detect DCIS via its CXCR4-expression levels. An important step herein will be the further ex vivo assessment of CXCR4-expression levels in existing human DCIS samples and their surrounding stroma and mammary gland tissue.

For a discussion regarding the tracer uptake and its relation to the degree of angiogenesis, see the Supporting Information.

Next to presence of the target, we found that the specificity of the signal in the tumor-lesions (see **Figure 2**) was greatly influenced by the time between injection and the SPECT measurements. Other than the data reported by De Silva et al. [33] and Nimmagadda et. al [11], who showed that the best results were obtained at 90 minutes after injection of [^{64}Cu]AMD3465 and [^{64}Cu]AMD3100, with ^{111}In-DTPA-Ac-TZ14011 no discrimination could be made between MIN-O and control tumors at 1 hour after injection (**Figure 1**). In our studies, a differentiation could, however, only be clearly made at 24 hours after injection. This suggests a high level of non-specific uptake of ^{111}In-DTPA-Ac-TZ14011 at 1 hour after injection. Hanaoka et al. previously evaluated the distribution of ^{111}In-DTPA-Ac-TZ14011 in a CXCR4 positive tumor model for pancreatic cancer [21] at different time points. They showed that tumor uptake was highest at 1 hour post injection, but that non-specific background was significantly decreased after 24 hours. Based on these findings We reasoned that at earlier time points (e.g. 1 hour and 6 hours [21]) there was still the possibility of presence of unbound compound in the tumor, which could decrease the overall visibility of the tumor. Therefore, 24 hours was considered to be the best imaging time point for this specific tracer. This time-span is still significantly shorter than the reported antibody based CXCR4-imaging approaches, which require a 48 hour incubation time [29]. A 24 hour incubation time, however, limits imaging studies to use of longer living isotopes such as ^{111}In and ^{89}Zr. The use of these isotopes in turn dictates the tracer design to include a chelate like DTPA.

The Ac-TZ14011 peptide provides a good platform for the development of imaging agents that are radiolabeled. Previously we have already shown that the peptide can also be used in combination with a fluorescent label [20] or a hybrid label [19].

Conclusions

IHC and flow cytometry validate that ^{111}In-DTPA-Ac-TZ14011 based imaging of CXCR4 receptor expression enables analysis of the longitudinal tumor lesion progression in a mouse model resembling human DCIS. Presence of CXCR4 positive lymphocytes and tumor-angiogenesis were shown to have little effect on the uptake of ^{111}In-DTPA-Ac-TZ14011 in the tumor.

Acknowledgements

This research is supported, by a KWF-translational research award (Grant No.PGF 2009-4344; FvL) and via FP7-HYPERImage (grant no. 201651; TB), a the National Center for Research resourcesgrant (K26 RR0243037;

ADB), and by the Molecular Imaging Research Program from the Ministry of Education, Culture, Sports, Science and Technology of Japan.

Address correspondence to: Dr. Fijs WB van Leeuwen, Department of Radiology, Interventional Molecular Imaging, Leiden University Medical Center (LUMC), Leiden, The Netherlands E-mail: F.W.B.van_Leeuwen@lumc.nl

References

[1] Donzella GA, Schols D, Lin SW, Esté JA, Nagashima KA, Maddon PJ, Allaway GP, Sakmar TP, Henson G, de Clercq E, Moore JP. AMD3100, a small molecule inhibitor of HIV-1 entry via the CXCR4 co-receptor. Nature Med 1998; 4: 71-7.

[2] Balkwill F. The significance of cancer cell expression of the chemokine receptor CXCR4. Seminars in Cancer Biology 2004; 14: 171-9.

[3] Balkwill F. Cancer and the chemokine network. Nature Rev Cancer 2004; 4: 540-550.

[4] Luker KE, Luker GD. Functions of CXCL12 and CXCR4 in breast cancer. Cancer Letters 2006; 238: 30-41.

[5] Epstein RJ. The CXCL12-CXCR4 chemotactic pathway as a target of adjuvant breast cancer therapies. Nature Rev Cancer 2004; 4: 1-9.

[6] Salvucci O, Bouchard A, Baccarelli A, Deschênes J, Sauter G, Simon R, Bianchi R, Basik M. The role of CXCR4 receptor expression in breast cancer: a large tissue microarray study. Breast Cancer Res Treat 2006; 97: 275-283.

[7] Schmid BC, Rudas M, Resniczek GA, Leodolter S, Zeillinger R. CXCR4 is expressed in ductal carcinoma in situ of the breast and in atypical ductal hyperplasia. Breast Cancer Res Treat 2004; 84: 247-250.

[8] Leonard GD, Swain SM. Ductal carcinoma in situ, complexities and challenges. J Natl Cancer Inst 2004; 96: 906-920.

[9] Irvine T, Fentiman IS. Biology and treatment of ductal carcinoma in situ. Expert Rev Anticancer Ther 2007; 7: 135-145.

[10] Virnig BA, Tuttle TM, Shanliyan T, Kane RL. Ductal carcinoma in situ of the breast: a systematic review of incidence, treatment, and outcomes. J Natl Cancer Inst 2010; 102: 170-178.

[11] Nimmagadda S, Pullambhatla M, Stone K, Green G, Bhujwalla ZM, Pomper MG. Molecular Imaging of CXCR4 receptor expression in human cancer xenografts with [64Cu] AMD3100 positron emission tomography. Cancer Res 2010; 70: 3935-3944.

[12] Jacobsen O, Weiss ID, Szajek L, Farber JM, Kiesewetter DO. 64Cu-AMD3100-A novel imaging agent for targeting chemokine receptor CXCR4. Bioorg Med Chem 2009; 17: 1486-1493.

[13] Tamamura H, Xu Y, Hattori T, Zhang X, Arakaki R, Kanbara K, Omagari A, Otaka A, Ibuka T, Yamamoto N, Nakashima H, Fujii N. A low-molecular-weight inhibitor against the chemokine receptor CXCR4: A strong anti-HIV peptide. Biochem Biophys Res Com 1998; 253: 877-882.

[14] Tamamura H, Hiramatsu K, Mizumoto M, Ueda S, Kusano S, Terakubo S, Akamatsu M, Yamamoto N, Trent J, Wang Z, Peiper S, Nakashima H, Otaka A, Fujii N. Enhancement of the T140-based pharmacophores leads to the development of more potent and bio-stable CXCR4 antagonists. Org Biomol Chem 2003; 1: 3663-3669.

[15] Tamamura H, Omagari A, Hiramatsu K, Gotoh K, Kanamoto T, Xu Y, Kodama E, Matsuoka M, Hattori T, Yamamoto N, Nakashima H, Otaka A, Fujii N. Development of specific CXCR4 inhibitors possessing high selectivity indexes as well as complete stability in serum based on an anti-HIV peptide T140. Bioorg Med Chem Lett 2001; 11: 1897-1902.

[16] Nomura W, Tanabe Y, Tsutsumi H, Tanaka T, Ohba K, Yamamoto N, Tamamura H. Fluorophore labeling enables imaging and evaluation of specific CXCR4-ligand interaction at the cell membrane for fluorescent based screening. Bioconjugate Chem 2008; 19: 1917-1920.

[17] Jacobsen O, Weiss ID, Kiesewetter DO, Farber JM, Chen X. PET of tumor CXCR4 expression with 4-18F-T140. J Nucl Med 2010; 51: 1796-1804.

[18] Nishizawa K, Nishiyama H, Oishi S, Tanahara N, Kotani H, Mikami Y, Toda Y, Evans BJ, Peiper SC, Saito R, Watanabe J, Fujii N, Ogawa O. Fluorescent imaging of high-grade bladder cancer using a specific antagonist for chemokine receptor CXCR4. Int J Cancer 2010; 127: 1180-1187.

[19] Kuil J Buckle T, Yuan H, van den Berg NS, Oishi S, Fujii N, Josephson L, van Leeuwen FWB. Synthesis and evaluation of a bimodal CXCR4 antagonistic peptide. Bioconjugate Chem 2011; 22: 859-864.

[20] van den Berg NS, Buckle T, Kuil J, Wesseling J, van Leeuwen FWB. Immunohistochemical detection of the CXCR4-expression in tumor tissue using the fluorescent peptide antagonist Ac-TZ14011-FITC. Transl Oncol 2011; 4: 224-230.

[21] Hanaoka H, Mukai T, Tamamura H, Mori T, Ishino S, Ogawa K, Iida Y, Doi R, Fujii N, Saji H. Development of a 111In-labeled peptide derivative targeting a chemokine receptor, CXCR4, for imaging tumors. Nucl Med Biol 2006; 33: 489-493.

[22] Maglione JE, McGoldrick ET, Young LJT,

Namba R, Gregg JP, Liu L, Moghanaki D, Ellies LG, Borowsky AD, Cardiff RD, MacLeod CL. Polyomavirus middle T-induced mammary intraepithelial neoplasiaoutgrowts: single origin, divergent evolution, and multiple outcomes. Mol Cancer Ther 2004; 3: 941-953.

[23] Abbey CK, Borowski AD, McGoldrick, Gregg JP, Maglione JE, Cardiff RD, Cherry SR. In vivo positron-emission tomography imaging of progression and transformation in a mouse model of mammary neoplasia. PNAS 2004; 101: 11438-11443.

[24] Namba R, Young LJT, Maglione JE, McGoldrick ET, Liu S, Wurz GT, DeGregorio, Borowsky AD, MacLeod CL, Cardiff RD, Gregg JP. Selective estrogen receptor modulators inhibit growth and progression of premalignant lesions in a mouse model of ductal carcinoma in situ. Breast Cancer Res 2005; 7: R881-889.

[25] Numba R, Maglione JE, Davis R, Baron CA, Liu S, Carmack CE, Young LJT, Borowsky AD, Cardiff RD, Gregg JP. Heterogeneity of mammary lesions represent molecular differences. BMC Cancer 2006; 6: 1-19.

[26] van Leeuwen FWB, Buckle T, Batteau L, Pool B, Sinaasappel M, Jonkers J, Gilhuijs KG. Potential value of color-coded dynamic breast-specific gamma-imaging; comparing (99m)Tc-(V)-DMSA, (99m)Tc-MIBI, and (99m)Tc-HDP in a mouse mammary tumor model. Appl Rad Isotopes 2010; 68: 2117-24.

[27] Nie Y, Waite J, Brewer F, Sunshine MJ, Littman DR, Zou YR. The role of CXCR4 in maintaining peripheral B cell compartments and humoral immunity. J Exp Med 2004; 9: 1145-1156.

[28] Beer AJ, Schwaiger M. Imaging of integrin α3β5 expression. Cancer Metastasis Rev 2008; 27: 631-644.

[29] Nimmagadda S, Pullaambhatla M, Pomper MG. Immuno imaging of CXCR4 expression in brain tumor xenografts using SPECT/CT. J Nucl Med 2009; 50: 1124-1130.

[30] Thurber GM, Weissleder R. Quantitating antibody uptake in vivo: Conditional dependence on antigen expression levels. Mol Imaging Biol 2011; 12: 623-632.

[31] Thurber GM, Schmidt MM, Wittrup KD. Antibody tumor penetration: Transport opposed by systemic and antigen-mediated clearance. Adv Drug Del Rev 2008; 60: 1421-1434.

[32] Sharkey RM, Karacay H, Cardillo TM, Chang CH, McBride WJ, Rossi EA, Horak ID, Goldenberg DM. Improving the delivery of radionuclides for imaging and therapy of cancer using pretargeting methods. Clin Cancer Res 2005; 11: 7109s-7121s.

[33] De Silva RA, Peyre K, Pullambhatla M, Fox JJ, Pomper MG, Nimmagadda S. Imaging CXCR4 expression in human cancer xenografts: evaluation of monocyclam 64Cu-AMD3465. J Nucl Med 2011; 52: 986-993.

Bioorganic & Medicinal Chemistry Letters 22 (2012) 2146–2150

Contents lists available at SciVerse ScienceDirect

Bioorganic & Medicinal Chemistry Letters

journal homepage: www.elsevier.com/locate/bmcl

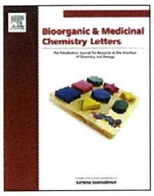

Molecular modeling study of cyclic pentapeptide CXCR4 antagonists: New insight into CXCR4–FC131 interactions

Yasushi Yoshikawa [a], Kazuya Kobayashi [b], Shinya Oishi [b], Nobutaka Fujii [b], Toshio Furuya [a,c,*]

[a] *Drug Discovery Department, Research & Development Division, PharmaDesign, Inc., 2-19-8 Hatchobori, Chuo-ku, Tokyo 104-0032, Japan*
[b] *Graduate School of Pharmaceutical Sciences, Kyoto University, Sakyo-ku, Kyoto 606-8501, Japan*
[c] *Open Innovation Center for Drug Discovery, The University of Tokyo, 7-3-1 Hongo, Bunkyo-ku, Tokyo 113-0033, Japan*

ARTICLE INFO

Article history:
Received 8 December 2011
Revised 27 January 2012
Accepted 31 January 2012
Available online 8 February 2012

Keywords:
FC131
CXCR4
GPCR
Docking
Molecular modeling

ABSTRACT

CXCR4 is a G-protein coupled receptor that is associated with many diseases such as breast cancer metastasis, HIV infection, leukemic disease and rheumatoid arthritis, and is thus considered an attractive drug target. Previously, we identified a cyclic pentapeptide, FC131, that is a potent antagonist for CXCR4. In this study, we constructed a three dimensional model of the CXCR4–FC131 complex. To investigate the backbone flexibility of FC131, we performed molecular dynamics simulations of FC131 based on the NMR structure of FC131, and obtained snapshot structures from the trajectories which were used to model the docking pose of FC131 into CXCR4. Our final model of the CXCR4–FC131 complex is partially different from the X-ray crystal structure of CXCR4–CVX15 and suggests water-mediated interactions. Nevertheless, this docking pose is consistent with the experimental data. We believe our model will aid in the discovery and development of small-molecule antagonists for CXCR4.

The chemokine receptors are a subfamily of G-protein coupled receptors (GPCRs) that bind to chemokines, a family of chemotactic factor proteins.[1,2] One chemokine receptor, CXCR4, binds CXCL12 (SDF-1α, stromal cell derived factor 1α), which engages the leukocyte chemotaxis in the immune system, progenitor cell migration,[3] and embryonic development of the cardiovascular,[4] hemopoietic,[5] and central nervous systems.[6,7] Moreover, CXCR4 is associated with many pathological physiologies such as breast cancer metastasis,[8] HIV infection,[9,10] leukemia and rheumatoid arthritis,[11] making CXCR4 an attractive target for drug discovery.

We previously identified several peptide antagonists for CXCR4. T140 (**1**) is a 14-residue cyclic peptide derived from the structure–activity relationship (SAR) studies of horseshoe crab antimicrobial peptides.[12,13] This peptide and its analogues are potent CXCR4 antagonists and act as HIV-1 entry inhibitors,[12] anti-cancer[14,15] and anti-rheumatoid agents.[16] FC131 (**2**) was identified from a cyclic-pentapeptide library whose design was based on SAR studies of T140 analogues (Fig. 1).[17] SAR studies of FC131 showed that the side chains of D-Tyr1, Arg3 and Nal4 are essential for ligand binding to CXCR4.[18,19]

In order to develop small-molecule CXCR4 antagonists based on these peptides, it is essential to understand the binding mode of the peptide ligands to CXCR4. To date, the three dimensional structures of FC131 and its analogues were revealed by in-house NMR studies.[18,19] The pharmacophore models and docking structure with CXCR4 by homology modeling have also been reported,[20–22] but building an accurate homology model of CXCR4 from other known GPCR structures is challenging due to the low amino acid sequence identity between CXCR4 and other known GPCR structures. However, the X-ray crystal structures of CXCR4–CVX15 (**3**) and CXCR4-IT1t (**4**) were recently determined[23]; this, together with the NMR structures of FC131 and its derivatives, allowed us to construct models of CXCR4 complexed with FC131 and its analogues.

First, to circumvent the fact that AutoDock4[24] cannot generate conformations of the FC131 backbone, we employed molecular dynamics (MD) simulations based on the previously reported NMR structures of FC131 and its analogues. This MD simulation allowed us to consider the conformational flexibility of the cyclic peptide backbone of FC131. Second, we docked CVX15 to determine the number of Lamarkian genetic algorithm (LGA). Third, using AutoDock4, we docked FC131, using the sampled structure from the MD trajectories, and investigated the binding mode and SAR of FC131 derivatives. The MD simulations and molecular manipulations were performed using MOE.[25] All MD simulations and docking calculations were performed on a Linux cluster system with Intel(R) Xeon(R) CPU E5440@2.83 GHz × 24 processors (96 cores).

AutoDock4 cannot generate conformations of macrocyclic frameworks of ligands. In consideration of the flexible FC131 backbone on AutoDock4, the MD simulations were applied based on the

---

[*] Corresponding author. Tel.: +81 3 3523 9630; fax: +81 3 3523 9631.
E-mail address: furuya@pharmadesign.co.jp (T. Furuya).

0960-894X/$ - see front matter © 2012 Elsevier Ltd. All rights reserved.
doi:10.1016/j.bmcl.2012.01.134

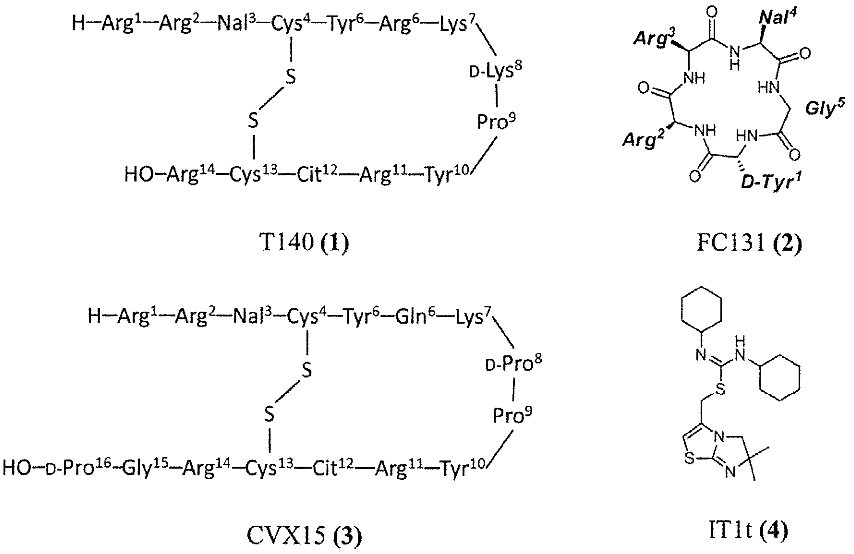

Figure 1. The structures of T140 (**1**), FC131 (**2**), CVX15 (**3**) and IT1t (**4**).

structures from in-house NMR studies, and the conformations were sampled from each trajectory. Although the backbone conformations were very similar, slight differences could cause relatively large side chain conformational variation in docking simulation (Fig. 1 in Supplementary data). Indeed, these sampling would search larger conformational space than that obtained without using MD during the docking simulation.

To determine the best parameters for AutoDock4 simulations, the number of individual LGA runs (ga_run) was set to 10, 200 and 20,000 to compare the accuracy of the output docking poses. The best scored output docking pose from each setting with CVX15 is shown in Figure 2 of the Supplementary data. The best docking pose did not fit to the binding mode of the crystal structure when the ga_run value was 10. The docking pose obtained by simulation when the ga_run value was 200 showed that the same binding pockets were occupied, but the position of Nal3 was flipped, and the best scored pose showed CXCR4 bound upside down. When the ga_run value was 20,000, the best ranked docking poses were the same as in the crystal structure. This indicates that the peptide binding energy function reproduced that of the crystal structure, making it suitable for docking to CXCR4. We postulated that the correct binding mode of FC131 to CXCR4 would be obtained when ga_run was set to an arbitrarily large number.

Using these results, we sampled 240 poses from MD simulation trajectories based on 12 NMR structures of FC131. The ga_run value of each sampled molecule was set to 1000. Based on the SAR studies, the arginine and naphthylalanine side chains of each ligand were essential for effective ligand binding. Therefore, the output docking poses were evaluated by calculating the shape score using ROCS.[26] The weighting parameter of the 'Color features' of ROCS for the hydrogen bond accepting Arg3 guanidino group and Nal4 naphthyl group were set to three. Finally, the best docking pose was selected by visual inspection and was optimized to generate the final model.

We compared the binding mode of the docking model of FC131 and the crystal structure of CVX15 (Fig. 2a). Because FC131 was identified from a library of cyclic pentapeptides that contain Nal, Tyr and two Arg residues derived from T140, FC131 may have an identical or similar binding mode to T140 and the related CVX15. The CXCR4–FC131 model complexes and the CVX15 coordinates are shown in Figure 2. The positions of L-Arg3 and L-Nal4 of FC131 superimpose well onto Arg2 and Nal3 of CVX15, but the other parts were not shared (Fig. 2a,b,c).

In our model, the L-Arg3 side chain of FC131 makes hydrogen bonds with His113$^{3.29}$, Thr117$^{3.33}$ and Asp171$^{4.60}$ of CXCR4 (Superscript according to the Ballesteros–Weinstein numbering scheme.[27] The residues in extracellular loop 2 were notated as 'ecl2'.). These interactions are the same as those of Arg2 in the CVX15 crystal structure (Fig. 2b). The side chain coordinates of L-Nal4 in FC131 are almost the same as that of Nal3 in CVX15. Although the backbone conformation of FC131 is similar to the NMR structures of FC131 (Fig. 3 in Supplementary data), different conformations of the amide bond between L-Arg3-L-Nal4 of FC131 and Arg2-Nal3 of CVX15 were observed. This may be due to the different position of the naphthalene substituent in FC131 (2-naphthyl) and CVX15 (1-naphthyl).

The FC131 D-Tyr1 and L-Arg2 side chains in the model occupy space adjacent to TM1, TM2 and TM7. (Fig. 2a, c) These positions in the binding pocket are not the same as in the bound form of CVX15, but coincide with binding pocket residues in the crystal structure of a small-molecule antagonist, IT1t structure (PDB code: 3OE6).[22] The D-Tyr1 side chain of FC131 extends into the pocket formed by Leu41$^{1.35}$, Tyr45$^{1.39}$, Trp94$^{2.60}$ and Ser285$^{7.36}$ of CXCR4. The hydroxyl group of D-Tyr1 forms a hydrogen bond with Tyr45$^{1.39}$. We previously showed that substitution of D-Tyr1 with Phe (**5**) in FC131 decreased binding.[28] Mutation studies also indicated that CXCR4 Tyr45$^{1.39}$ and the corresponding residues in other chemokine receptors are important for ligand binding.[29–32] These results indicate that possible polar interactions between the hydroxyl groups of FC131 D-Tyr1 and CXCR4 Tyr45$^{1.39}$ contribute to ligand–receptor binding. The guanidino group of L-Arg2 in FC131 forms polar interactions with the side chains of Asp97$^{2.64}$ and Asp187^{ecl2} in CXCR4. Although CVX15 does not occupy the pocket containing Asp97$^{2.64}$ in CXCR4, some mutational analyses indicate that Asp97$^{2.64}$ is essential for binding potent small-molecule CXCR4 ligands.[29,33] The crystal structure of CXCR4 shows that the small-molecule antagonist IT1t also interacts with Asp97$^{2.64}$.[23] CXCR4 Asp187^{ecl2} is involved in binding SDF-1,[33] and interacts with Arg1 of CVX15 through polar interactions in the crystal structure. The backbone carbonyl oxygen of FC131 L-Arg2 interacts with the backbone nitrogen of CXCR4 Arg188^{ecl2}. This interaction is also observed in the CXCR4–CVX15 structure. Additionally, the back-

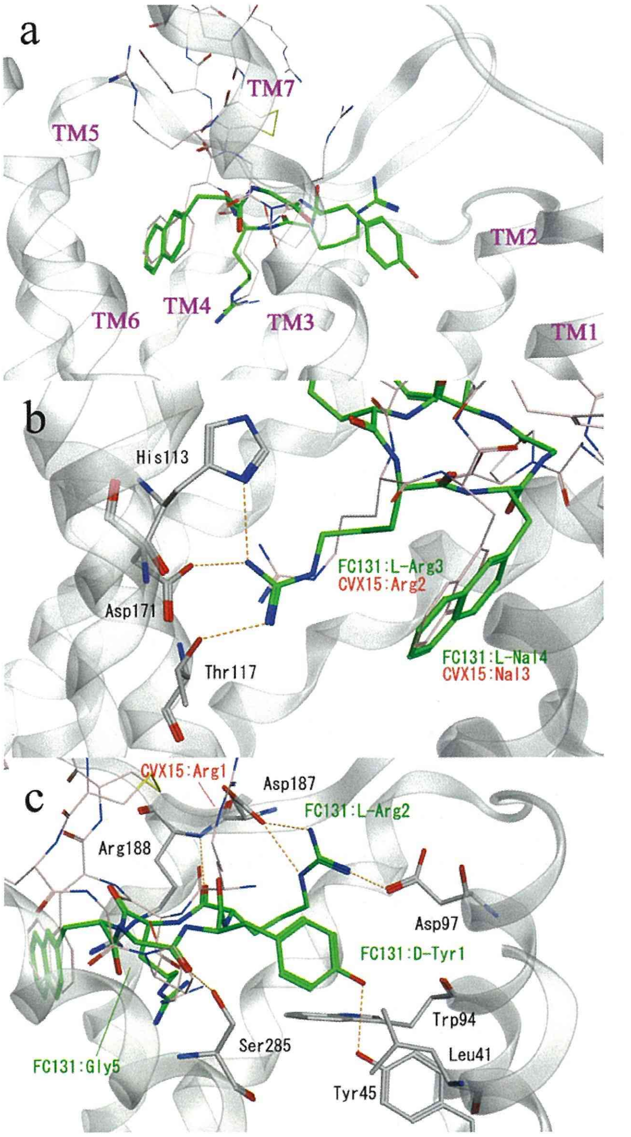

Figure 2. Comparison of the docking poses between FC131 and CVX15. (a) Overall docking pose of FC131. (b) The interaction between L-Arg3 and L-Nal4 of FC131 and CXCR4. (c) The interaction between D-Tyr1 and L-Arg2 of FC131. FC131 is shown as green sticks, CVX15 is shown as pink lines, and CXCR4 residues are shown as white sticks. The backbone structures of CXCR4 are shown in ribbon representation.

bone carbonyl oxygen of FC131 Gly5 makes polar interactions with CXCR4 Ser285$^{7.36}$ (Fig. 2c).

Mutation studies showed that CXCR4 Asp262$^{6.58}$ is an important residue for ligand binding.[34] In the reported crystal structure, the Arg14 side chain in CVX15 is close to CXCR4 Asp262$^{6.58}$. In contrast, our docking study indicates that the two Arg side chains in FC131 are not in this position. CXCR4 Glu288$^{7.39}$ is another essential residue for ligand binding.[32] Although CVX15 does not directly interact with Glu288$^{7.39}$, a hydrogen bond via a water molecule is observed. In a similar fashion to CVX15, interaction of FC131 with Glu288$^{7.39}$ of CXCR4 is mediated by a hydrogen bond network that includes two water molecules (**w1** and **w2**, Fig. 3a). Following energy minimization of the CXCR4–FC131 model complex with the water molecules observed in the crystal structure of the CXCR4–CVX15 complex, the L-Nal4 carbonyl oxygen in FC131, and the Glu288$^{7.39}$ side chain and the Tyr255$^{6.51}$ hydroxyl group in CXCR4, formed a hydrogen bond network via a water molecule (**w1**). Alternatively, the amide nitrogen of FC131 L-Arg2 makes a hydrogen bond network with CXCR4 Glu288$^{7.39}$ through a water molecule (**w2**) which also makes an OH–π interaction with the D-Tyr1 aromatic moiety of FC131 (Fig. 3a).

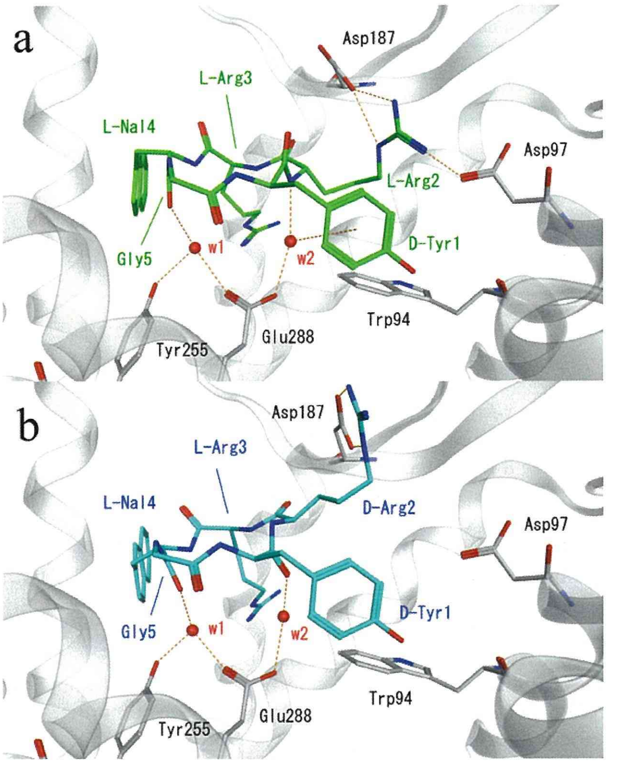

Figure 3. The water-mediated interactions between CXCR4 and the ligands. (a) Binding mode of FC131 with CXCR4. (b) Binding mode of peptide **8**. The carbon atoms of FC131 and compound **8** are shown in green and cyan, respectively. The backbone structures of CXCR4 are shown in ribbon representation. **w1** and **w2** are water molecules from the crystal structure.

Our previous studies on the NMR structure of FC131 suggested that FC131 and its derivatives exhibit several backbone conformations.[19] The NMR structure of L-Ala5-substituted peptide (**6**) has a flipped amide bond linking L-Nal4-L-Ala5 as compared to FC131, while the D-Ala5 substituent (**7**) has the same backbone conformation as FC131. The D-Arg2 substituted FC131 derivative (**8**) also has a flipped amide bond, linking D-Tyr1-D-Arg2. On the other hand, the D-*N*-methylarginine (D-MeArg) substituent (**10**) shows the same backbone conformation as FC131. These conformational differences are summarized in Table 1. We next investigated the possible binding mode of these derivatives in the context of SAR.

Peptide **6** has over 40-fold lower potency and peptide **7** has threefold lower potency compared to FC131. In our model, the peptide bond between L-Nal4 and Gly5 of FC131 makes a hydrogen bond network with Tyr255$^{6.51}$ and Glu288$^{7.39}$, mediated by water molecule **w1** as described above. The flipped conformation of the L-Nal4-L-Ala5 peptide bond in **6** breaks this hydrogen bond network with **w1**, resulting in the decreased potency of **6**. In contrast, peptide **7** retains both the hydrogen bond network of FC131 and binding affinity to CXCR4. The differences in the potencies between peptides 6 and 7 may be attributed to the differences in the conformations around Nal4 and Ala5.

Peptide **8** has only two times lower activity than FC131, in spite of relatively large structural changes. The docking model of **8** was constructed by modifying the CXCR4–FC131 model complex. The optimized model is shown in Figure 3b. The backbone of **8** is slightly moved towards the extracellular region compared with

Table 1
CXCR4 binding affinities of FC131 analogues[a]

ID	Sequence	IC$_{50}$ (μM)	Comparison of the backbone conformation with FC131.
2 (FC131)	*cyclo*(-D-Tyr^1-L-Arg^2-L-Arg^3-L-Nal^4-Gly^5-)	0.004	–
5	*cyclo*(-D-*Phe*^{1}-L-Arg^2-L-Arg^3-L-Nal^4-Gly^5-)	0.051	–
6	*cyclo*(-D-Tyr^1-L-Arg^2-L-Arg^3-L-Nal^4-L-*Ala*^{5}-)	0.17	Flipped direction of the amide bond between L-Nal^4-L-Ala^5
7	*cyclo*(-D-Tyr^1-L-Arg^2-L-Arg^3-L-Nal^4-D-*Ala*^{5}-)	0.011	Same amide bond directions
8	*cyclo*(-D-Tyr^1-D-*Arg*^{2}-L-Arg^3-L-Nal^4-Gly^5-)	0.008	Flipped direction of the amide bond between D-Tyr^1-D-Arg^2
9	*cyclo*(-D-Tyr^1-L-*MeArg*^{2}-L-Arg^3-L-Nal^4-Gly^5-)	0.023	–
10	*cyclo*(-D-Tyr^1-D-*MeArg*^{2}-L-Arg^3-L-Nal^4-Gly^5-)	0.003	Same amide bond directions
11	*cyclo*(-D-Tyr^1-L-*Lys*^{2}-L-Arg^3-L-Nal^4-Gly^5-)	0.097	–
12	*cyclo*(-D-Tyr^1-L-*Ala*^{2}-L-Arg^3-L-Nal^4-Gly^5-)	0.063	–

[a] Values are taken from our previous reports.[18,19]

FC131. The D-Arg2 side chain in **8** extends into the extracellular space to interact with only CXCR4 Asp187^{ecl2}. The guanidino group of D-Arg2 in **8** forms two hydrogen bonds with the Asp187^{ecl2} side chain of CXCR4 and does not form any unfavorable contacts. This is in contrast with the L-Arg2 side chain in FC131, which is buried in the space between Asp97$^{2.64}$ and Asp187^{ecl2} of CXCR4 (Fig. 3a). The contributions of water molecule **w2** to the hydrogen bond network in FC131 binding was also supported by the SAR data. An L-MeArg2 substitution (**9**) exhibits sixfold lower potency than FC131, which may be attributable to the disturbed hydrogen bond between L-Arg2 NH and **w2**. On the other hand, epimer peptide **10** containing D-MeArg2 has twice the potency of peptide **8** containing D-Arg2. Because a hydrogen bond network via **w2** was originally formed with the D-Tyr1 carbonyl oxygen in **8**, N-methylation on the peptide bond did not affect any hydrogen bond network and thus does not affect receptor binding. Although previous NMR study demonstrated that the orientation of the D-Tyr1-D-MeArg2 peptide bond in **10** is the same as that of FC131 in solution, the binding mode of peptide **10** with CXCR4 should be similar to peptide **8**.

L-Lys2 substitution (**11**) and L-Ala2 substitution (**12**) of FC131 cause a 24- and 16-fold decrease in potency, respectively. In our docking model, the L-Arg2 side chain of FC131 is packed tightly into the space comprised by Asp97$^{2.64}$ and Asp187^{ecl2} of CXCR4. Therefore, substitution of this guanidine group affects binding significantly, so slight modifications to the side chain result in significantly decreased potency. On the other hand, in the docking model of D-Arg2 substituted peptide (**8**), the D-Arg2 pocket is positioned close to the extracellular region of CXCR4 and thus does not interact tightly with CXCR4, so modification of D-Arg2 would be less effective than modification of L-Arg2. Recently, a molecular modeling study using the X-ray structure of CXCR4 was reported.[35] The authors built models of CXCR4 complexed with a dimeric peptide ligand, in which D-Arg2 of **8** was modified with D-ornithine (D-Orn) to conjugate the two cyclic pentapeptide ligands for dimerization. Although their binding modes for the peptides were different from our model, the position of D-Orn in their model was the same as that of D-Arg2 of **8** in our model. The side chains were extended into the extracellular region and interacted with Asp187^{ecl2}. This indicates Arg2 of peptide 8 may have a tolerance for substitution.

In conclusion, we have described a binding model of the CXCR4–FC131 complex obtained using NMR structures of FC131, molecular dynamics simulations, and docking analyses. In the optimized model, the side chain coordinates of L-Arg3 and L-Nal4 in FC131 correspond to Arg2 and Nal3, respectively, in CVX15. Interestingly, D-Tyr1 and L-Arg2 in FC131 did not share the binding pockets for CVX15. The different binding modes of FC131 and CVX15, which include water-mediated hydrogen bonds, are consistent with the experimental data. The SAR among several FC131 analogues are also explained by the docking model. This model will be useful for understanding the binding mode of CXCR4–ligand complexes and for the design of novel CXCR4 antagonists.

Acknowledgments

This work was supported by Targeted Proteins Research Program. K.K. is grateful to the JSPS Research Fellowships for Young Scientists.

Supplementary data

Supplementary data associated with this article can be found, in the online version, at doi:10.1016/j.bmcl.2012.01.134.

References and notes

1. Mackay, C. R. *Nat. Immunol.* **2001**, *2*, 95.
2. Murphy, P. M.; Baggiolini, M.; Charo, I. F.; Hébert, C. A.; Horuk, R.; Matsushima, K.; Miller, L. H.; Oppenheim, J. J.; Power, C. A. *Pharmacol. Rev.* **2000**, *52*, 145.
3. Nagasawa, T.; Hirota, S.; Tachibana, K.; Takakura, N.; Nishikawa, S.; Kitamura, Y.; Yoshida, N.; Kikutani, H.; Kishimoto, T. *Nature* **1996**, *382*, 635.
4. Tachibana, K.; Hirota, S.; Iizasa, H.; Yoshida, H.; Kawabata, K.; Kataoka, Y.; Kitamura, Y.; Matsushima, K.; Yoshida, N.; Nishikawa, S.; Kishimoto, T.; Nagasawa, T. *Nature* **1998**, *393*, 591.
5. Aiuti, A.; Webb, I. J.; Bleul, C.; Springer, T.; Gutierrez-Ramos, J. C. *J. Exp. Med.* **1997**, *185*, 111.
6. Stumm, R. K.; Zhou, C.; Ara, T.; Lazarini, F.; Dubois-Dalcq, M.; Nagasawa, T.; Höllt, V.; Schulz, S. *J. Neurosci.* **2003**, *23*, 5123.
7. Zhu, Y.; Yu, T.; Zhang, X.-C.; Nagasawa, T.; Wu, J. Y.; Rao, Y. *Nat. Neurosci.* **2002**, *5*, 719.
8. Zhu, Y.; Yu, T.; Zhang, X.-C.; Nagasawa, T.; Wu, J. Y.; Rao, Y. *Nat. Neurosci.* **2002**, *5*, 719.
9. Feng, Y.; Broder, C. C.; Kennedy, P. E.; Berger, E. A. *Science* **1996**, *272*, 872.
10. Oberlin, E.; Amara, A.; Bachelerie, F.; Bessia, C.; Virelizier, J. L.; Arenzana-Seisdedos, F.; Schwartz, O.; Heard, J. M.; Clark-Lewis, I.; Legler, D. F.; Loetscher, M.; Baggiolini, M.; Moser, B. *Nature* **1996**, *382*, 833.
11. Nanki, T.; Hayashida, K.; El-Gabalawy, H. S.; Suson, S.; Shi, K.; Girschick, H. J.; Yavuz, S.; Lipsky, P. E. *J. Immunol.* **2000**, *165*, 6590.
12. Tamamura, H.; Xu, Y.; Hattori, T.; Zhang, X.; Arakaki, R.; Kanbara, K.; Omagari, A.; Otaka, A.; Ibuka, T.; Yamamoto, N.; Nakashima, H.; Fujii, N. *Biochem. Biophys. Res. Commun.* **1998**, *253*, 877.
13. Tamamura, H.; Omagari, A.; Oishi, S.; Kanamoto, T.; Yamamoto, N.; Peiper, S. C.; Nakashima, H.; Otaka, A.; Fujii, N. *Bioorg. Med. Chem. Lett.* **2000**, *10*, 2633.
14. Takenaga, M.; Tamamura, H.; Hiramatsu, K.; Nakamura, N.; Yamaguchi, Y.; Kitagawa, A.; Kawai, S.; Nakashima, H.; Fujii, N.; Igarashi, R. *Biochem. Biophys. Res. Commun.* **2004**, *320*, 226.
15. Tamamura, H.; Hori, A.; Kanzaki, N.; Hiramatsu, K.; Mizumoto, M.; Nakashima, H.; Yamamoto, N.; Otaka, A.; Fujii, N. *FEBS Lett.* **2003**, *550*, 79.
16. Tamamura, H.; Fujisawa, M.; Hiramatsu, K.; Mizumoto, M.; Nakashima, H.; Yamamoto, N.; Otaka, A.; Fujii, N. *FEBS Lett.* **2004**, *569*, 99.
17. Fujii, N.; Oishi, S.; Hiramatsu, K.; Araki, T.; Ueda, S.; Tamamura, H.; Otaka, A.; Kusano, S.; Terakubo, S.; Nakashima, H.; Broach, J. A.; Trent, J. O.; Wang, Z.-xuan; Peiper, S. C. *Angew. Chem., Int. Ed.* **2003**, *42*, 3251.
18. Tamamura, H.; Araki, T.; Ueda, S.; Wang, Z.; Oishi, S.; Esaka, A.; Trent, J. O.; Nakashima, H.; Yamamoto, N.; Peiper, S. C.; Otaka, A.; Fujii, N. *J. Med. Chem.* **2005**, *48*, 3280.
19. Ueda, S.; Oishi, S.; Wang, Z.-xuan; Araki, T.; Tamamura, H.; Cluzeau, J.; Ohno, H.; Kusano, S.; Nakashima, H.; Trent, J. O.; Peiper, S. C.; Fujii, N. *J. Med. Chem.* **2007**, *50*, 192.
20. Våbenø, J.; Nikiforovich, G. V.; Marshall, G. R. *Biopolymers* **2006**, *84*, 459.
21. Våbenø, J.; Nikiforovich, G. V.; Marshall, G. R. *Chem. Biol. Drug Des.* **2006**, *67*, 346.
22. Kawatkar, S. P.; Yan, M.; Gevariya, H.; Lim, M. Y.; Eisold, S.; Zhu, X.; Huang, Z.; An, J. *Exp. Biol. Med. (Maywood)* **2011**, *236*, 844.

23. Wu, B.; Chien, E. Y. T.; Mol, C. D.; Fenalti, G.; Liu, W.; Katritch, V.; Abagyan, R.; Brooun, A.; Wells, P.; Bi, F. C.; Hamel, D. J.; Kuhn, P.; Handel, T. M.; Cherezov, V.; Stevens, R. C. *Science* **2010**, *330*, 1066.
24. Morris, G. M.; Huey, R.; Lindstrom, W.; Sanner, M. F.; Belew, R. K.; Goodsell, D. S.; Olson, A. J. *J. Comput. Chem.* **2009**, *30*, 2785.
25. Molecular Operating Environment (MOE), Chemical Computing Group Inc., Montreal, QC (Canada).
26. ROCS, version 3.0, OpenEye Scientific Software, Sanra Fe, NM, 2009.
27. Ballesteros, J.; Weinstein, H. *Methods Neurosci.* **1995**, *25*, 366.
28. Tamamura, H.; Esaka, A.; Ogawa, T.; Araki, T.; Ueda, S.; Wang, Z.; Trent, J. O.; Tsutsumi, H.; Masuno, H.; Nakashima, H.; Yamamoto, N.; Peiper, S. C.; Otaka, A.; Fujii, N. *Org. Biomol. Chem.* **2005**, *3*, 4392.
29. Wong, R. S. Y.; Bodart, V.; Metz, M.; Labrecque, J.; Bridger, G.; Fricker, S. P. *Mol. Pharmacol.* **2008**, *74*, 1485.
30. de Mendonça, F. L.; da Fonseca, P. C. A.; Phillips, R. M.; Saldanha, J. W.; Williams, T. J.; Pease, J. E. *J. Biol. Chem.* **2005**, *280*, 4808.
31. Berkhout, T. A.; Blaney, F. E.; Bridges, A. M.; Cooper, D. G.; Forbes, I. T.; Gribble, A. D.; Groot, P. H. E.; Hardy, A.; Ife, R. J.; Kaur, R.; Moores, K. E.; Shillito, H.; Willetts, J.; Witherington, J. *J. Med. Chem.* **2003**, *46*, 4070.
32. Dragic, T.; Trkola, A.; Thompson, D. A.; Cormier, E. G.; Kajumo, F. A.; Maxwell, E.; Lin, S. W.; Ying, W.; Smith, S. O.; Sakmar, T. P.; Moore, J. P. *Proc. Natl. Acad. Sci. U.S.A.* **2000**, *97*, 5639.
33. Brelot, A.; Heveker, N.; Montes, M.; Alizon, M. *J. Biol. Chem.* **2000**, *275*, 23736.
34. Gerlach, L. O.; Jakobsen, J. S.; Jensen, K. P.; Rosenkilde, M. R.; Skerlj, R. T.; Ryde, U.; Bridger, G. J.; Schwartz, T. W. *Biochemistry* **2003**, *42*, 710.
35. Demmer, O.; Dijkgraaf, I.; Schumacher, U.; Marinelli, L.; Cosconati, S.; Gourni, E.; Wester, H.-J.; Kessler, H. *J. Med. Chem.* **2011**, *54*, 7648.

Journal of
Medicinal
Chemistry

Article

pubs.acs.org/jmc

Structure–Activity Relationship Study of a CXC Chemokine Receptor Type 4 Antagonist, FC131, Using a Series of Alkene Dipeptide Isosteres

Kazuya Kobayashi,[†] Shinya Oishi,*[,†] Ryoko Hayashi,[†] Kenji Tomita,[†] Tatsuhiko Kubo,[†] Noriko Tanahara,[†] Hiroaki Ohno,[†] Yasushi Yoshikawa,[‡] Toshio Furuya,[‡] Masaru Hoshino,[†] and Nobutaka Fujii*[,†]

[†]Graduate School of Pharmaceutical Sciences, Kyoto University, Sakyo-ku, Kyoto 606-8501, Japan
[‡]PharmaDesign Inc., Chuo-ku, Tokyo 104-0032, Japan

Supporting Information

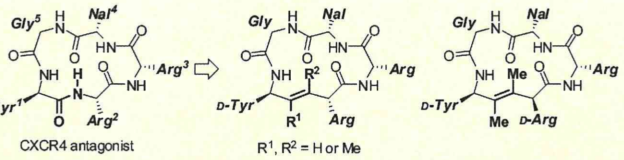

ABSTRACT: A structure–activity relationship study on a highly potent CXC chemokine receptor type 4 (CXCR4) antagonist, FC131 [cyclo(-D-Tyr^1-Arg^2-Arg^3-Nal^4-Gly^5-)], was carried out using a series of alkene isosteres of the D-Tyr^1-L/D-Arg^2 dipeptide to investigate the binding mode of FC131 and its derivatives with CXCR4. The structure–activity relationships of isostere-containing FC131 analogues were similar to those of the parent FC131 and its derivatives, suggesting that a *trans*-conformer of the D-Tyr^1–Arg^2 peptide bond is the dominant contributor to the bioactive conformations of FC131. Although NMR analysis demonstrated that the two conformations of the peptidomimetic containing the D-Tyr^1-D-Arg^2 isostere are possible, binding-mode prediction indicated that the orientations of the alkene motif within D-Tyr^1-MeArg^2 peptidomimetics depend on the chirality of Arg^2 and the β-methyl group of the isostere unit, which makes the dominant contribution for binding to the receptor. The most potent FC122 [cyclo(-D-Tyr^1-D-MeArg^2-Arg^3-Nal^4-Gly^5-)] bound with CXCR4 by a binding mode different from that of FC131.

INTRODUCTION

Cyclic peptides provide versatile scaffolds for the development of therapeutic agents in drug discovery from peptide ligands.[1] The cyclic structure provides several advantages, including preorganized conformations to improve the affinity for the target molecule(s),[2] protection from proteolytic degradation by exopeptidases,[3] and increased membrane permeability.[4,5] The restricted conformations can facilitate the identification of preferred spatial distributions of functional groups necessary for bioactivity. Cyclic peptides therefore offer promising lead compounds for optimization of small-molecule ligands via improvement of the bioactivity and/or selectivity in ligand-based drug design.[6] For example, Kessler and co-workers developed a cyclic RGD pentapeptide for highly potent antagonists of $\alpha_v\beta_3$ integrin.[7] The subsequent structure–activity relationship (SAR) studies identified a more potent and selective cyclic peptide.[8] Using information on the spatial distributions of the pharmacophoric elements of cyclic RGD peptides, small-molecule inhibitors with a variety of druglike scaffolds have been developed.[9−12] Endothelin receptor antagonists,[13−15] endomorphin-1 analogues,[16,17] and somatostatin analogues[18,19] with cyclic peptide scaffolds have also been exemplified.

Previously, we developed a highly potent CXC chemokine receptor type 4 (CXCR4) antagonist, FC131 [cyclo(-D-Tyr^1-Arg^2-Arg^3-Nal^4-Gly^5-)], from a library of cyclic pentapeptides consisting of pharmacophore residues of the polyphemusin-II-derived anti-human immunodeficiency virus (HIV) peptide T140.[20] Since this novel scaffold for CXCR4 antagonists was identified, a series of cyclic peptides and peptidomimetics have been designed for potential anti-HIV and antimetastatic agents.[21] For example, substitution of Arg^2 in FC131 with D-Arg and/or *N*-methylarginine (MeArg) provided interesting insights into SARs:[22] (1) the D-Arg^2-substituted derivative (FC092) showed slightly less potent activity than FC131 did, (2) in the low-energy structures of FC092, the orientation of the D-Tyr^1–D-Arg^2 peptide bond was flipped (Figure 1a,b), (3) the MeArg^2-substituted peptide (FC162) is less potent than FC131 is, (4) the D-MeArg^2-substituted peptide (FC122) is the most potent, and approximately 30% of the *N*-methylamide bonds in D-Tyr^1-D-MeArg^2 exist as the *cis*-conformer, and (5) the local conformation around D-Tyr^1-D-MeArg^2 in FC122 is similar to that of FC131 (Figure 1a,c). The D-Tyr^1-Arg^2 substructure in FC131 is therefore involved in direct or indirect contributions to binding with CXCR4. The different biological effects among the derivatives are likely to be derived from two possible pseudo-1,3-allylic strains between the Arg^2 side chain and the D-Tyr^1 carbonyl group and between the D-Tyr^1 side chain and the *N*-methyl group of MeArg^2; these can affect the orientations of the peptide bond (Figure 1b,c). In this study, we investigated the electrostatic and steric effects around

Received: December 15, 2011
Published: February 21, 2012

dx.doi.org/10.1021/jm2016914 | *J. Med. Chem.* 2012, 55, 2746−2757